Supplementary Information

Customized composition of lithium metal solid-electrolyte interphase by electric field modulation of anion motion direction

Shengtao Xu[1, +], Lijun Zheng[2, +], Xiaoyu Guo[1], Rong Gu[1], Shuaiqi Gong[1,3]*, Jinting Xu[1,3]*, Sheng Zhu[1,3]*, Qingwei Gao[1,3], Qunjie Xu[1,3], Penghui Shi[1,3], Xin Zhao[4], Yulin Min[1,3]*, Jun Lu[2]*

[1]Shanghai Key Laboratory of Materials Protection and Advanced Materials in Electric Power, Shanghai University of Electric Power, Shanghai 200090, China

[2]College of Chemical and Biological Engineering, Zhejiang University, Hangzhou, China

[3]Shanghai Institute of Pollution Control and Ecological Security Shanghai 200092, China

[4]College of Electrical Power Engineering, Shanghai University of Electric Power, Shanghai 200090, China

[+]These authors contributed equally

* E-mail: sq_gong@shiep.edu.cn (S.-Q. Gong), xujinting011291@shiep.edu.cn (J.-T. Xu), zhusheng@shiep.edu.cn (S. Zhu), minyulin@shiep.edu.cn (Y.-L. Min), junzoelu@zju.edu.cn (J. Lu).

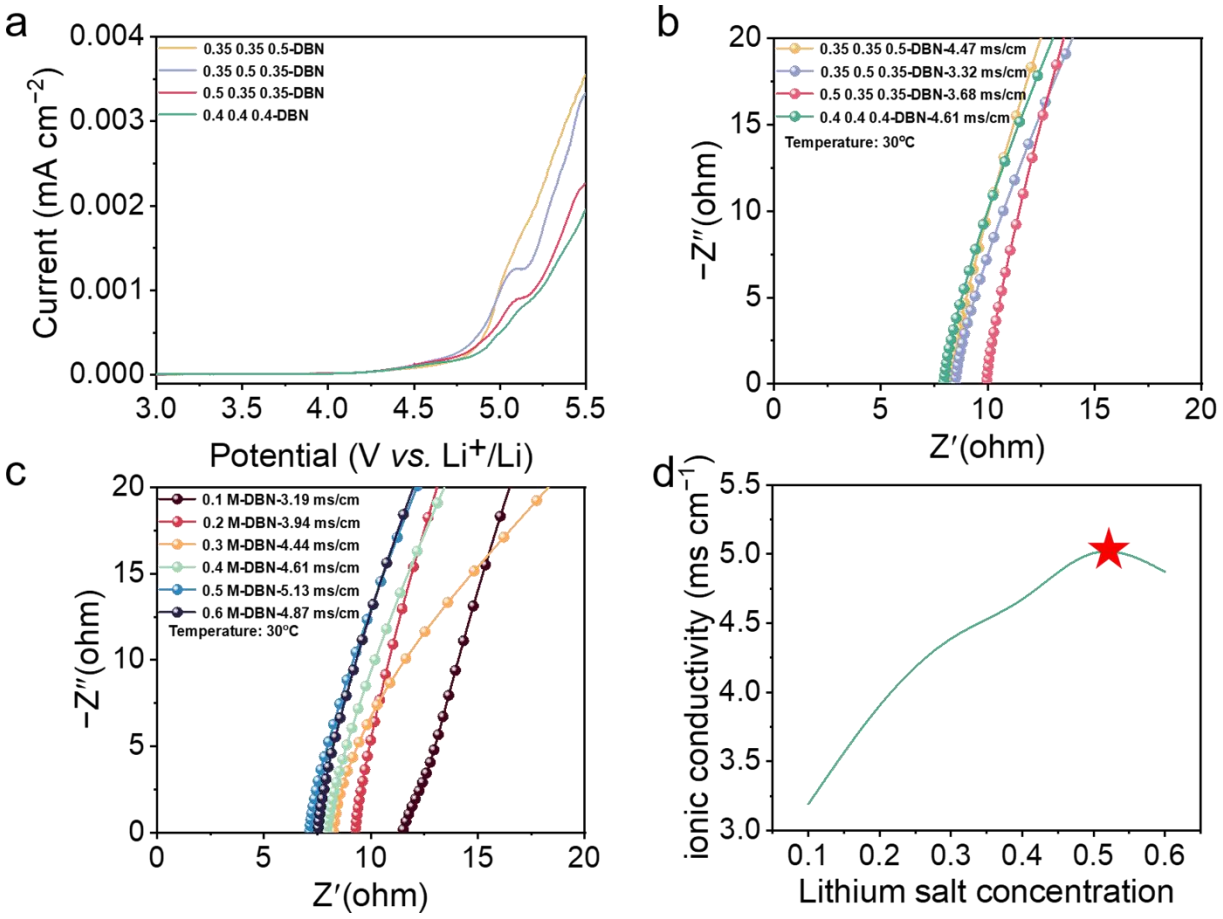

Figure S1. Systematic screening of the electrolyte formulation with an optimum ratio. (a) Oxidative stability of various electrolytes in various proportional formulations at a total concentration of 1.2 M. (b) Ionic conductivity of various electrolytes in different proportions of formulations with a total concentration of 1.2 M. (c) The Nyquist plots of XMol-DBN electrolytes. (d) The Li^+ conductivity of XMol-DBN electrolytes.

A comprehensive comparison of the oxidative stability and Li^+ conductivity of different electrolytes with different ratio formulations, with a total concentration of 1.2 M in (a) and (b), revealed that the electrolyte with a lithium salt ratio of 1:1:1 exhibited the most promising results. Further comparison of the Li^+ conductivity of the XM-DBN electrolyte revealed that 0.5M-DBN was selected as the optimal electrolyte formulation.

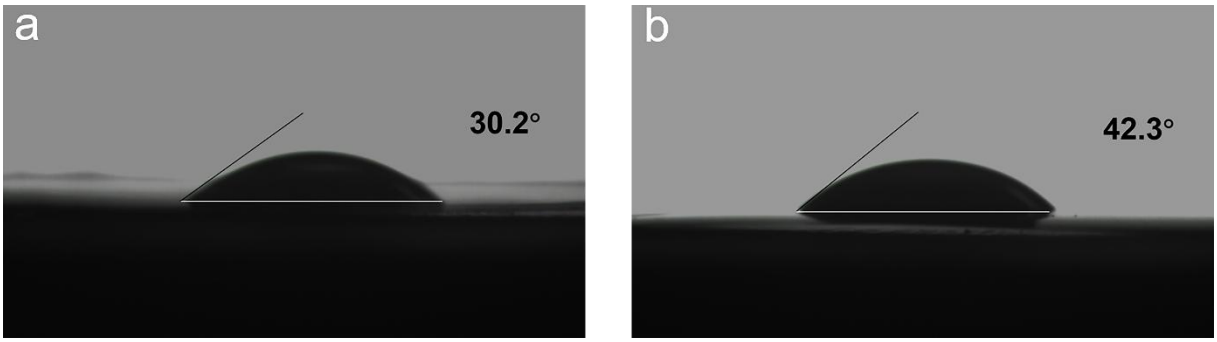

Figure S2. The contact angles of 0.5 M-DBN (a) and 1 M $LiPF_6$ EC/DMC (b) electrolytes with the separator.

The contact angle of 0.5 M-DBN is 30.2º, which is lower than that of 1 M $LiPF_6$ EC/DMC, further proving the wetting enhancement ability of 0.5 M-DBN on a separator

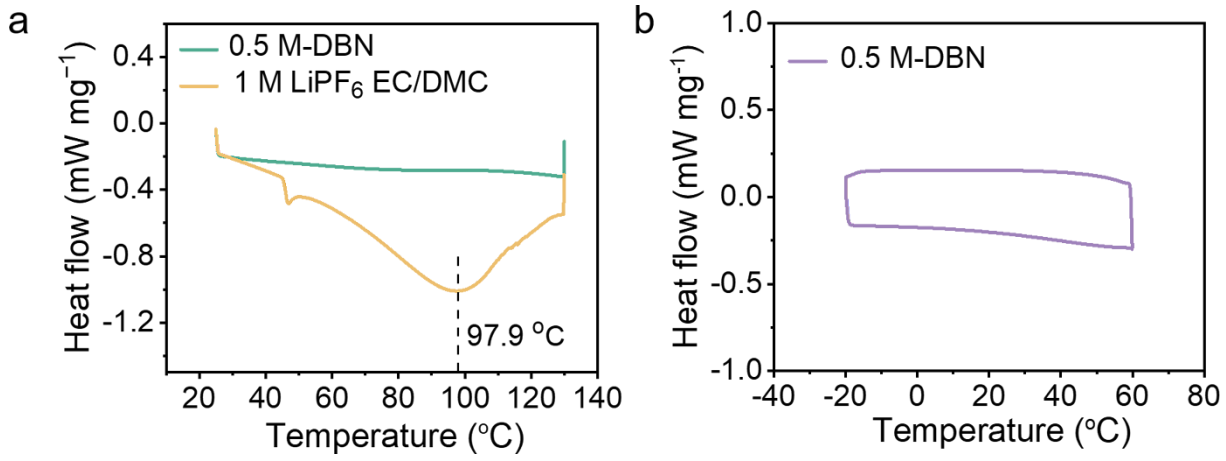

Figure S3. (a) Differential scanning calorimetry (DSC) warming curves for different electrolytes. The electrolytes were heated from room temperature (20°C) to 130°C at a rate of 5 °C/min. (b) DSC cooling and heating curves of 0.5 M-DBN electrolyte at a rate of 5 °C/min.

The 1 M $LiPF_6$ EC/DMC electrolyte undergoes volatilization at temperatures above 97.9 °C with a heat absorption peak. However, the 0.5 M-DBN electrolyte remained free of heat absorption peaks even when the temperature was cooled down to 130 °C, indicating its potential for high-temperature applications (Figure S5a). The results of the study showed that no obvious physical phase changes were observed in the 0.5 M-DBN sample in the temperature range from −20 °C to 60 °C, indicating that the electrolyte has a wide range of operating temperatures (Figure S5b).

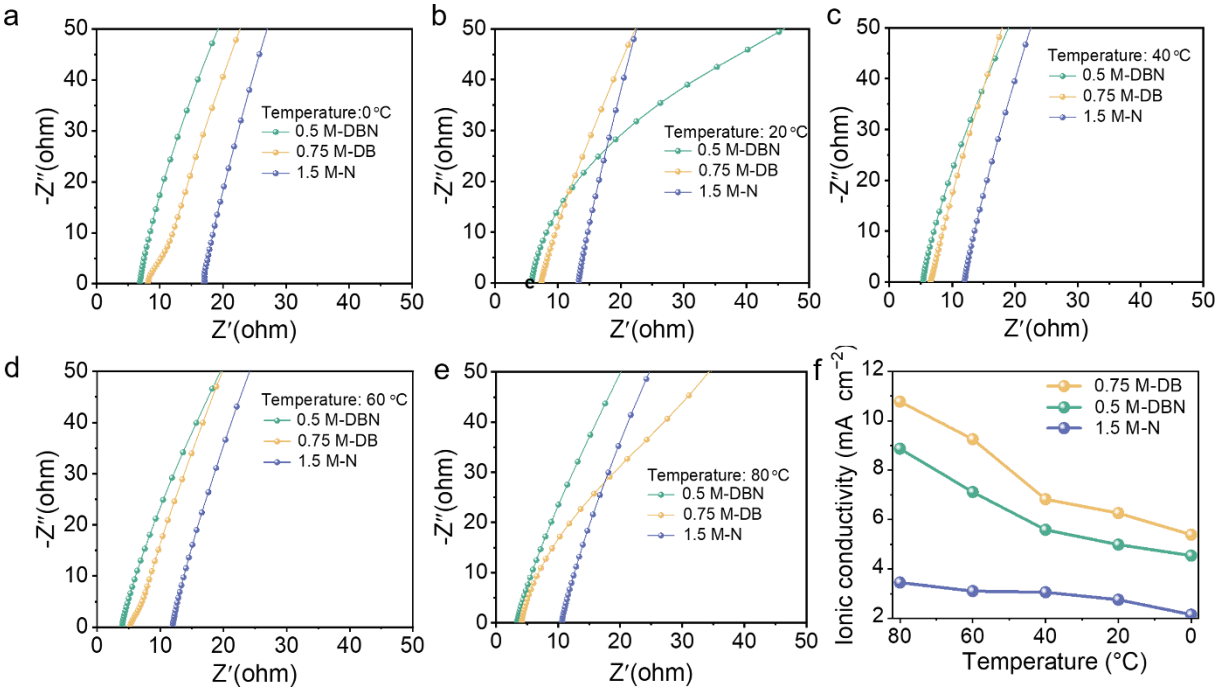

Figure S4. Nyquist plots of 0.5 M-DBN, 0.75 M-DB, and 1.5 M-N electrolytes at 0°C (a), 20°C (b), 40°C (c), 60°C (d), and 80°C (e). (f) The ionic conductivity at the aforementioned temperatures.

The results showed that the ionic conductivities of 0.5 M-DBN, 0.75 M-DB, and 1.5 M-N at 20 °C were 4.98 ms cm^{-1}, 6.26 ms cm^{-1}, and 2.75 ms cm^{-1}, respectively. Although ionic Although the 0.5 M-DBN electrolyte is not as good as the 0.75 M-DBN, its ionic conductivity close to 5 ms cm^{-1} is already at the upper end of the range of published nonflammable electrolytes (Table S3).

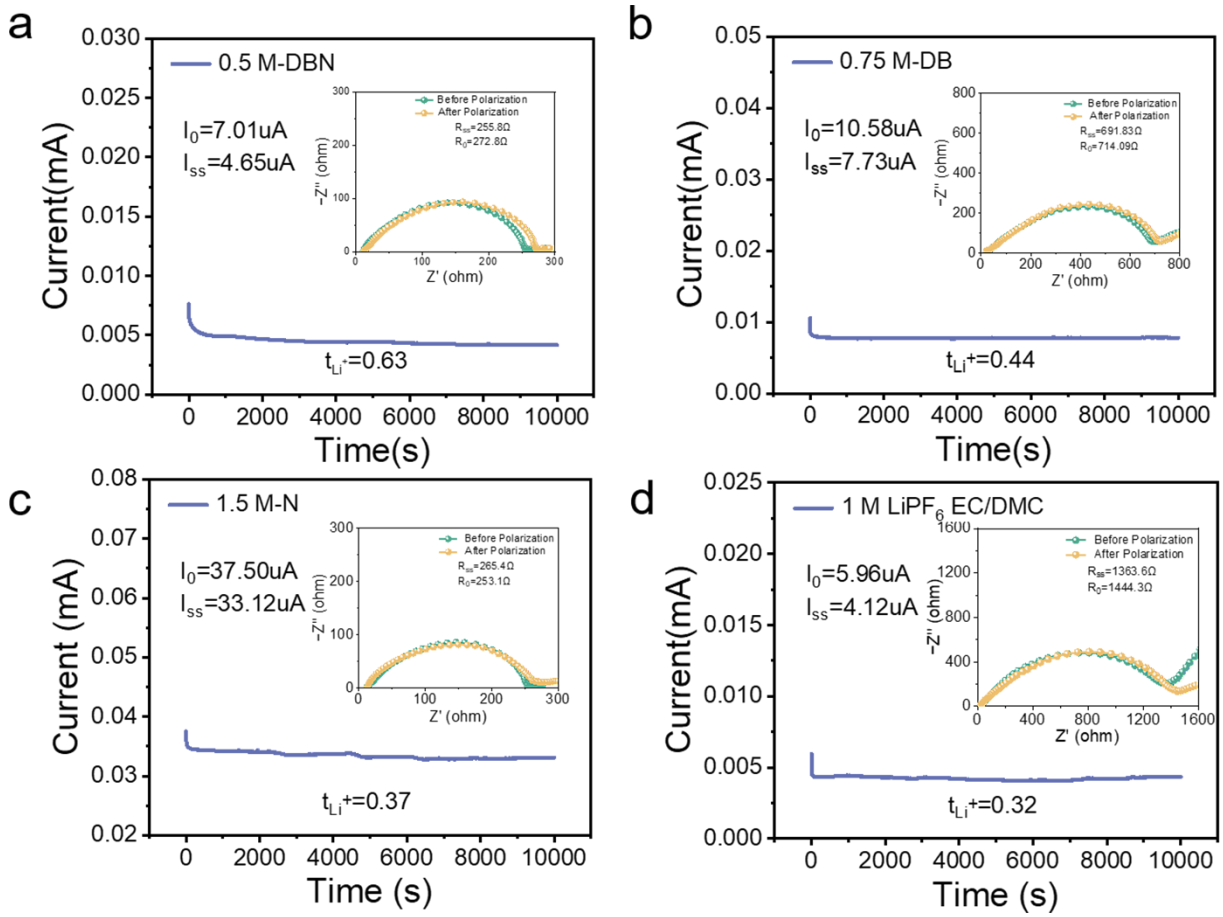

Figure S5. Polarization curves of cells with (a)0.5 M-DBN, (b)0.75 M-DB, (c)1.5 M-N, and (d)1 M $LiPF_6$ EC/DMC electrolytes at initial and steady state. The inset shows the impedance spectra in the initial and steady state.

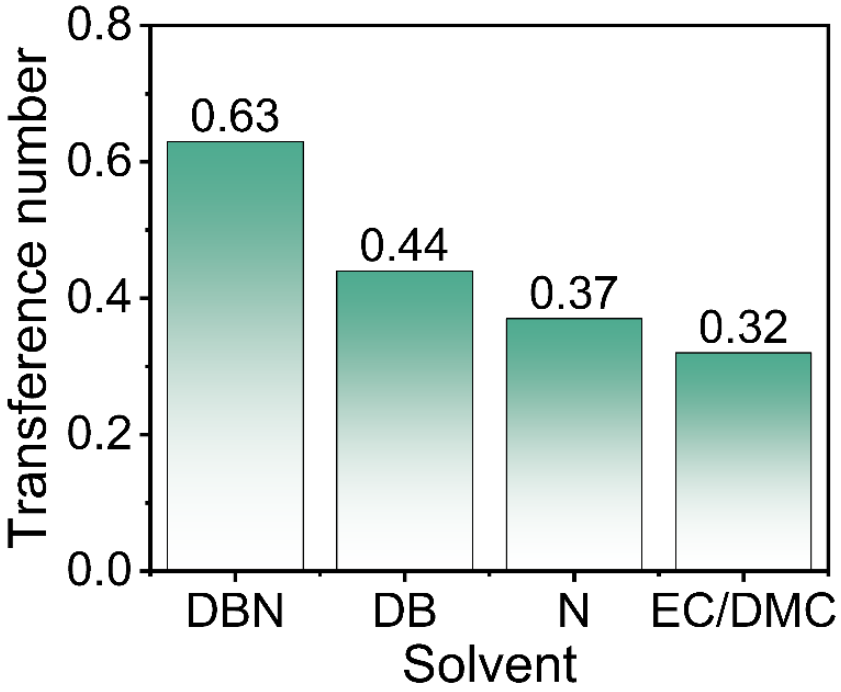

64

65 **Figure S6.** Four types of electrolyte ion migration numbers.

66

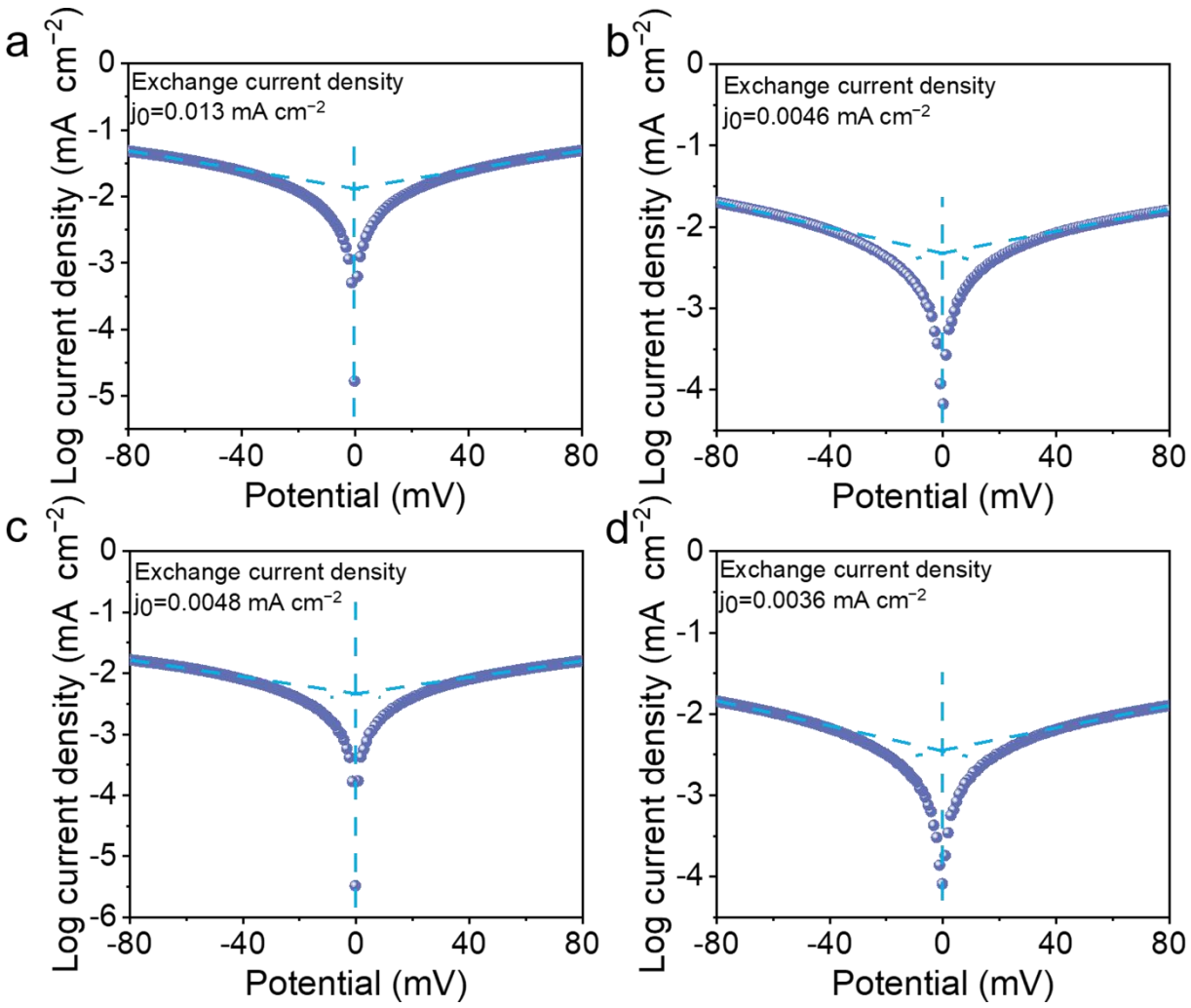

Figure S7. Tafel curves of Li/Li symmetric cells with 0.5 M-DBN (a), 0.75 M-DB (b), 1.5 M-N (c), and 1 M $LiPF_6$ EC/DMC (d) electrolytes at a temperature of 0°C.

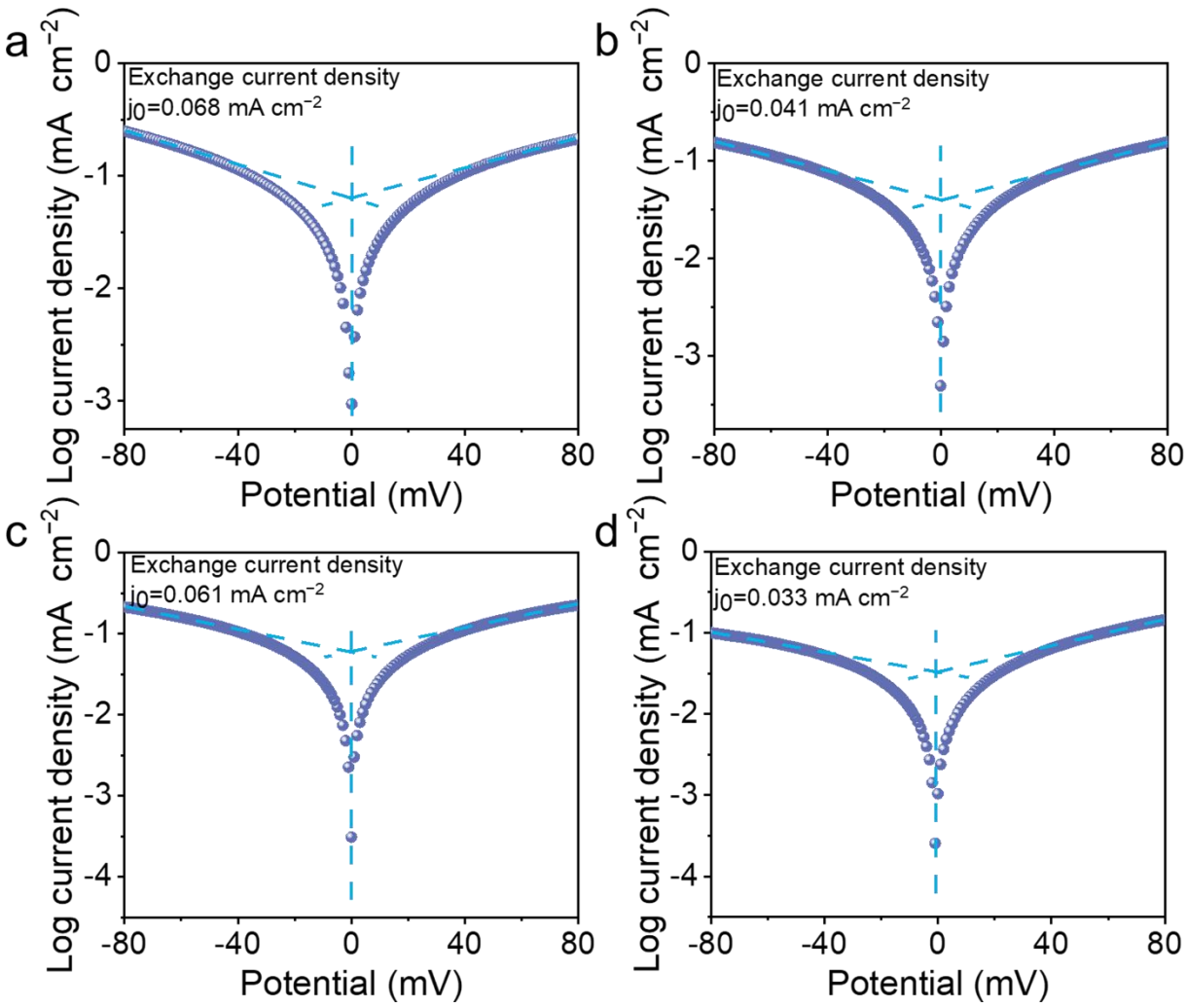

Figure S8. Tafel curves of Li/Li symmetric cells with 0.5 M-DBN (a), 0.75 M-DB (b), 1.5 M-N (c), and 1 M $LiPF_6$ EC/DMC (d) electrolytes at a temperature of 20°C.

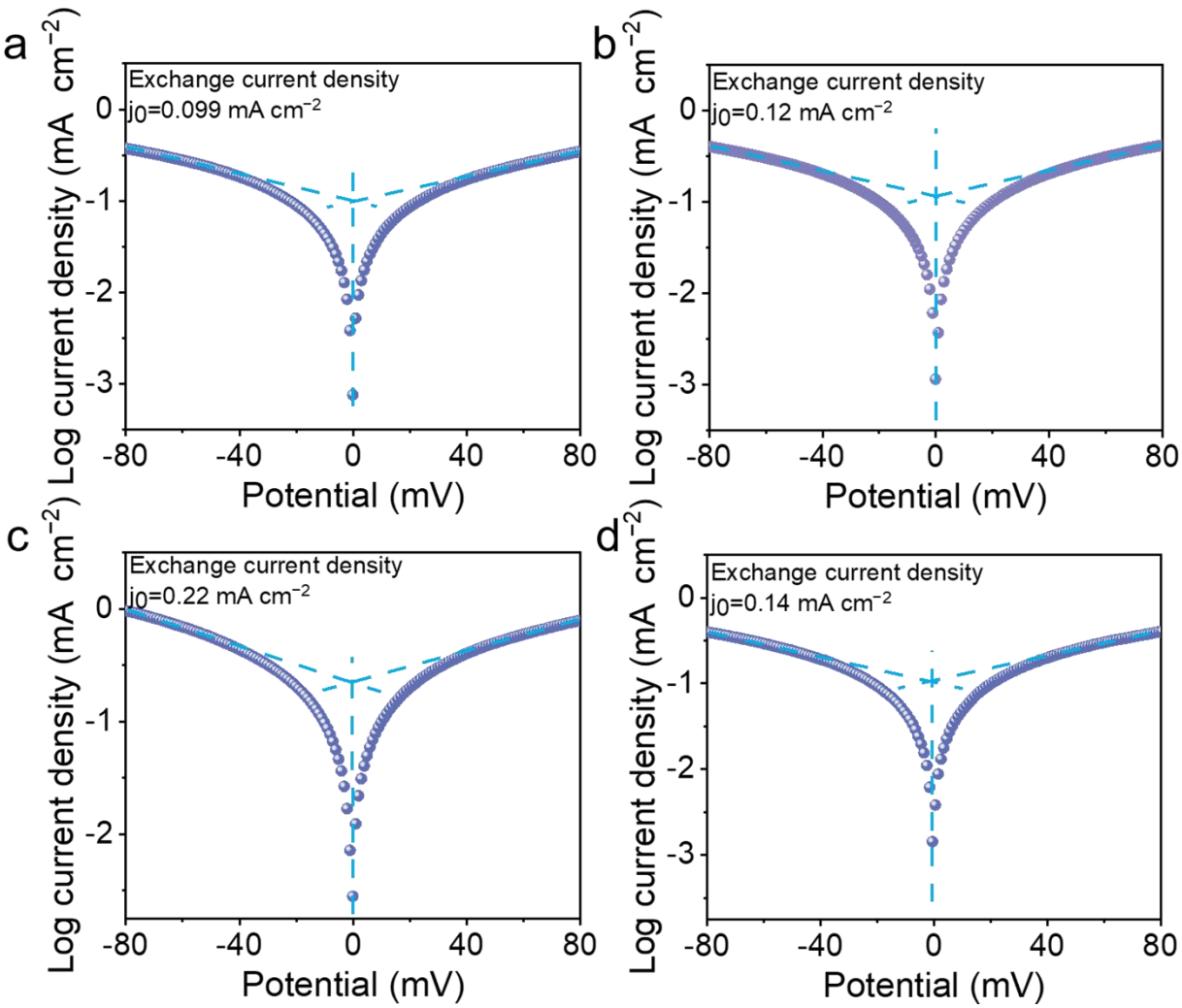

Figure S9. Tafel curves of Li/Li symmetric cells with 0.5 M-DBN (a), 0.75 M-DB (b), 1.5 M-N (c), and 1 M $LiPF_6$ EC/DMC (d) electrolytes at a temperature of 40°C.

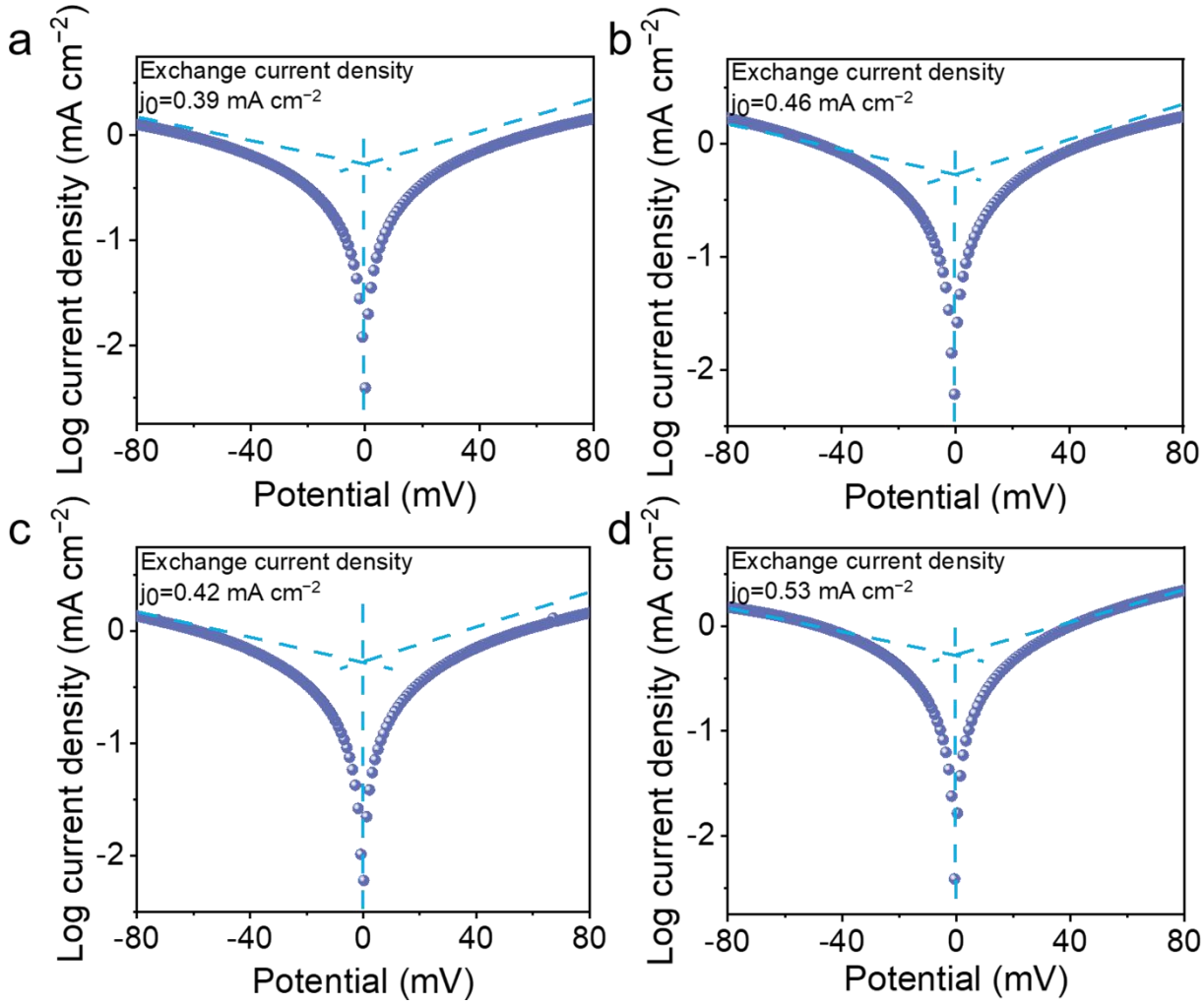

Figure S10. Tafel curves of Li/Li symmetric cells with 0.5 M-DBN (a), 0.75 M-DB (b), 1.5 M-N (c), and 1 M $LiPF_6$ EC/DMC (d) electrolytes at a temperature of 60°C.

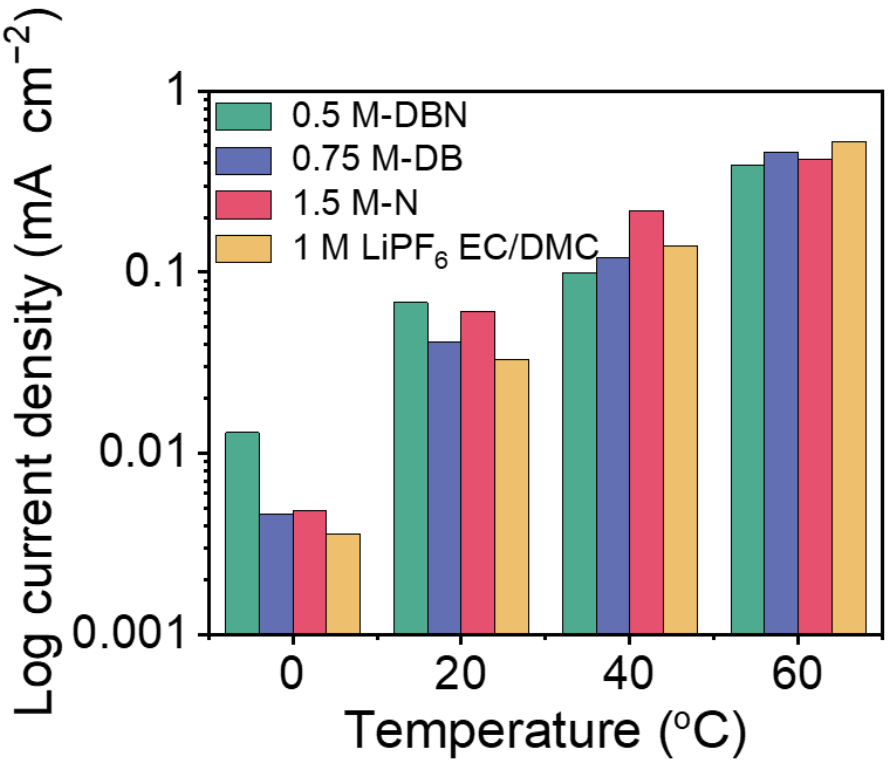

Figure S11. Exchange current density at each temperature.

Tafel curve tests at different temperatures to calculate the exchange current density to evaluate the interfacial reaction rate (Fig S8~S11). Notably, the 0.5 M-DBN electrolyte exhibited the largest exchange current densities of 0.013 mA cm^{-2} and 0.068 mA cm^{-2} at 0 °C and 20 °C, respectively, while the smallest exchange current densities at 40 °C and 60 °C were 0.099 mA cm^{-2} and 0.39 mA cm^{-2}, respectively. According to Arrhenius' law, the chemical reaction rate increases with increasing temperature. Therefore, high temperatures result in higher exchange current densities. However, too high a current density promotes the growth of lithium dendrites. On the other hand, at lower temperatures, higher exchange current densities are required to achieve the deposition and stripping of lithium ions at the interface. Therefore, 0.5 M-DBN electrolyte maintains an appropriate range of exchange current densities at both high and low temperatures, ensuring efficient and stable cell operation at both high and low temperatures.

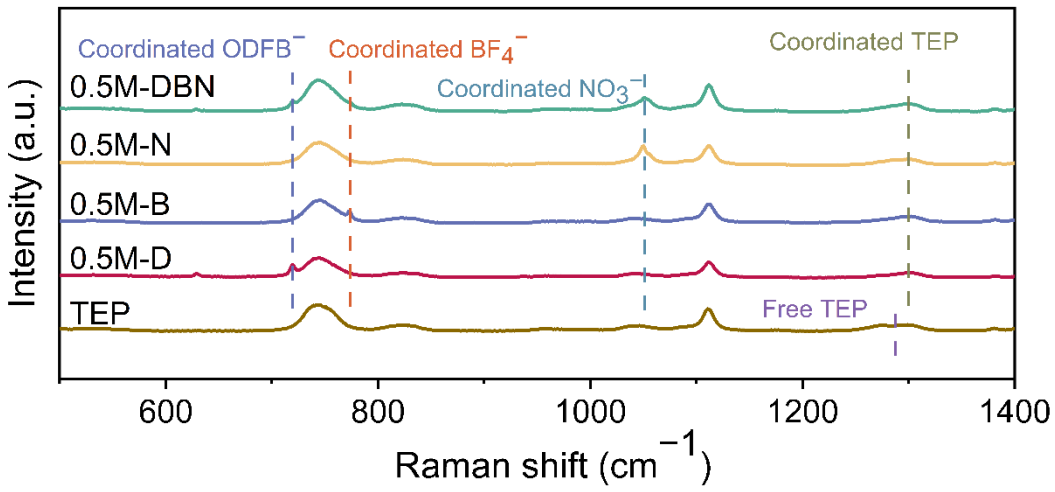

Figure S12. Raman spectra of electrolytes.

To investigate the solvation structure of the electrolyte, we analyzed the effect of three salts on the electrolyte using Raman spectroscopy (Figure. S12). As a control, we also examined TEP as a solvent and an electrolyte containing 1.5 M-D, 1.5 M-B, and 1.5 M-N. In the pure TEP solvent, we observed a peak at approximately 1288 cm^{-1}, which corresponds to the stretching vibration of the P=O bond. However, after the addition of the lithium salt, the peak of the stretching vibration of the P=O bond in the four samples shifted to about 1300 cm^{-1} due to the formation of the Li^{+}-TEP ligand. Interestingly, when the three salts were introduced into the electrolyte simultaneously, new peaks appeared that were caused by three different anions: $DFOB^{-}$ (720 cm^{-1}), BF_4^{-} (773 cm^{-1}), and NO_3^{-} (1050 cm^{-1}). These results indicate that the three salts affect the solvated structure by entering the solvated shell, forming peaks corresponding to the different anions.

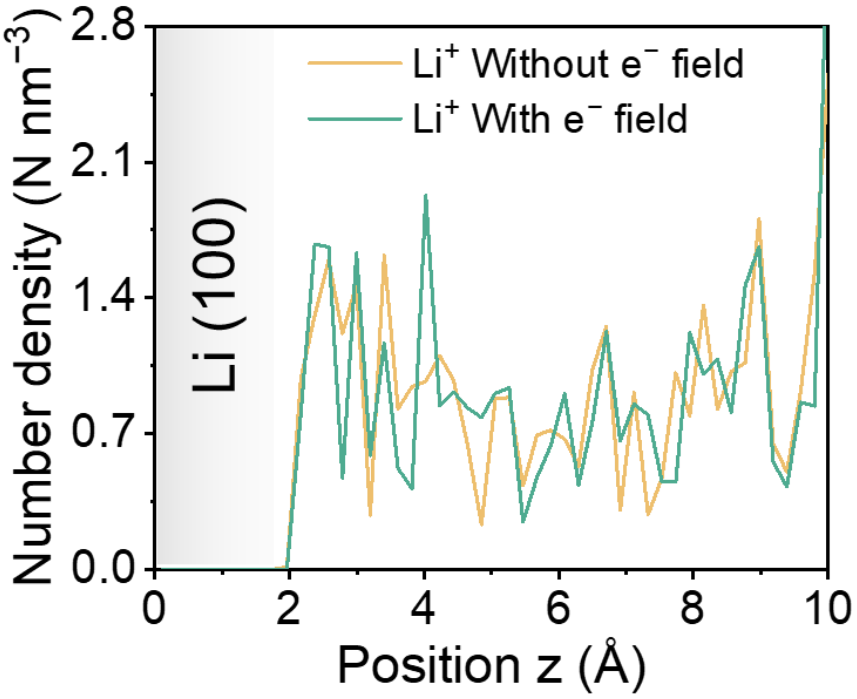

111

112 **Figure S13.** Number distribution of lithium ions in the Z-direction with and without an electric

113 field.

114

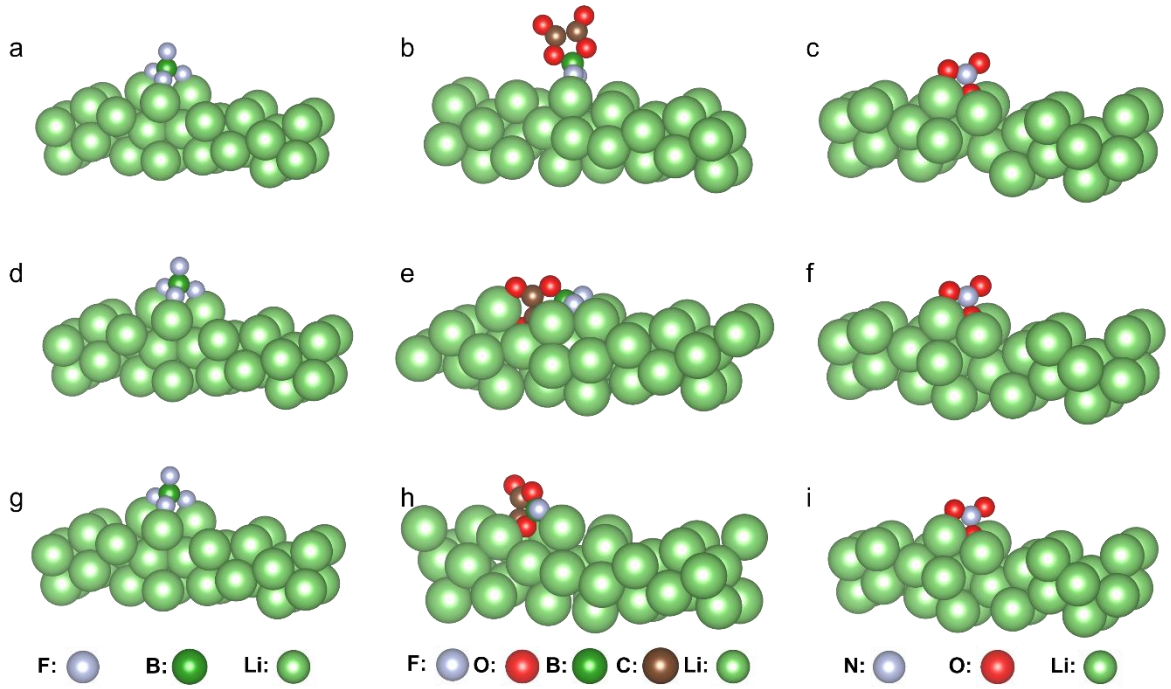

Figure S14. The adsorption energy calculations of three lithium salts — $LiBF_4$ (a, d, g), LiODFB (b, e, h), and $LiNO_3$ (c, f, i) — under three applied electric field conditions: 0 V/nm (a, b, c), −0.1 V/nm (d, e, f), and −1 V/nm (g, h, i).

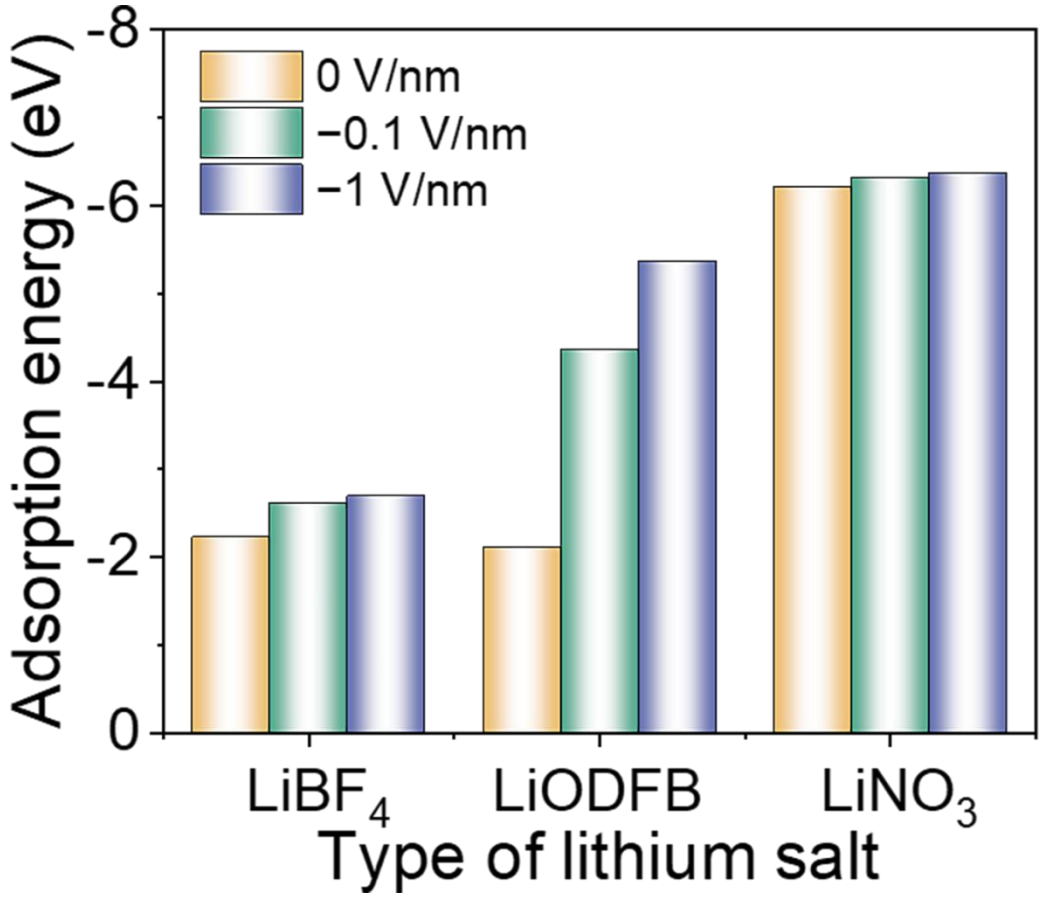

Figure S15. Adsorption energies of different lithium salts under various voltage conditions

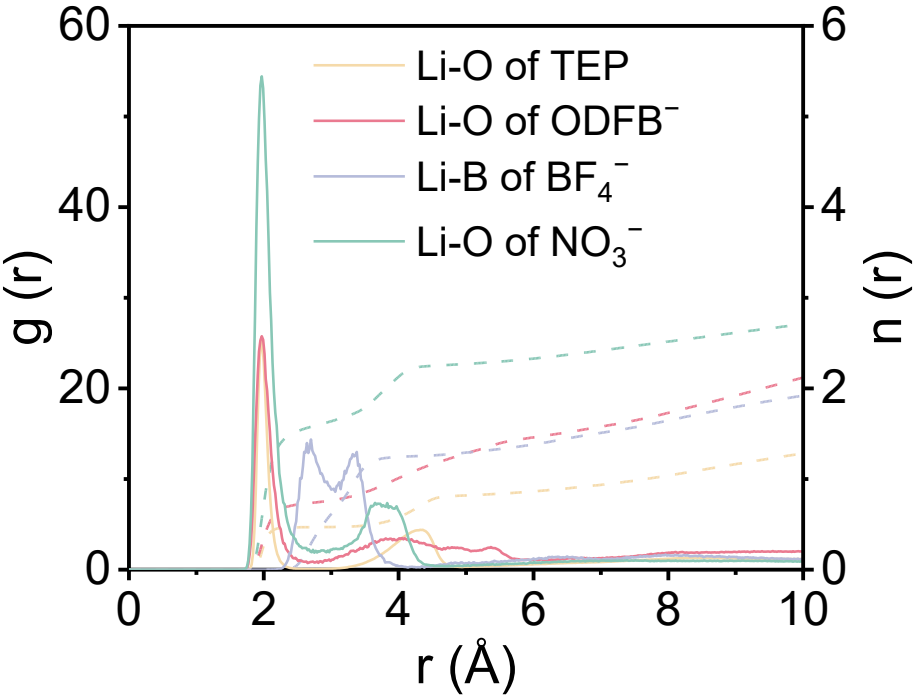

Figure S16. The corresponding radial distribution function of Li^+ in 0.5 M-DBN electrolyte in the case of electric field was obtained by MD simulation.

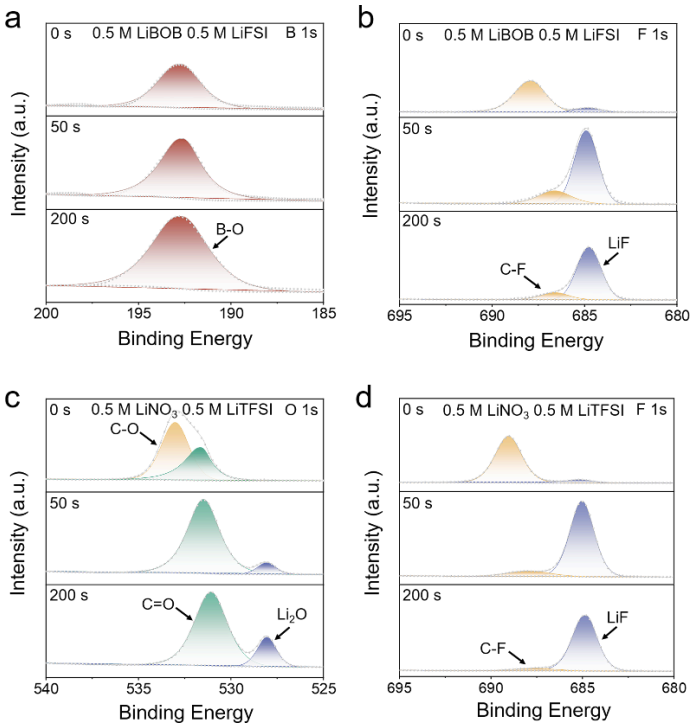

Figure S17. (a) B1s and (b) F1s XPS spectra of the SEI formed in the 0.5 M LiBOB + 0.5 M LiFSI TEP electrolyte. (c) O1s and (d) F1s XPS spectra of the SEI formed in the 0.5 M $LiNO_3$ + 0.5 M LiTFSI TEP electrolyte.

In the first set, a 0.5 M LiBOB + 0.5 M LiFSI TEP-based electrolyte was employed (LiBOB exhibits a higher binding energy than LiFSI). According to our theoretical predictions, LiBOB is expected to reside closer to the lithium surface and preferentially decompose, forming a B–O-rich inner SEI layer, while the weaker-binding LiFSI contributes to a LiF-rich outer SEI. Sputtering XPS analysis of the SEI composition (Fig. S15a) fully confirms the presence of this layered structure. In the second set, a 0.5 M $LiNO_3$ + 0.5 M LiTFSI TEP electrolyte was used ($LiNO_3$ has a higher binding energy than LiTFSI). Theoretical predictions suggest that $LiNO_3$ preferentially decomposes on the Li surface, forming a Li_2O-rich inner SEI (Li_2O was selected as a marker to exclude the influence of nitrogen from LiTFSI), while LiTFSI forms a LiF-dominated outer SEI. Sputtering XPS results (Fig. S15b) again confirm this spatial distribution.

These findings collectively demonstrate that the anion gradient distribution mechanism we proposed is not a system-specific phenomenon, but rather a general interfacial regulation principle.

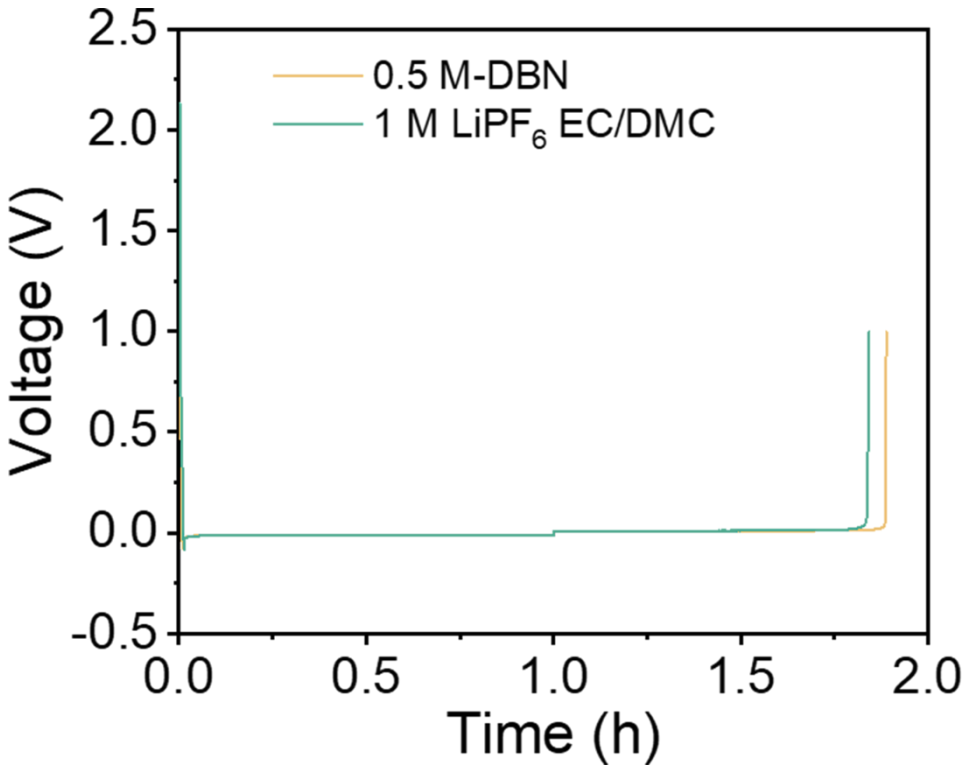

Figure S18. The plating and stripping curves of Li-Cu cell during the in-situ FT-IR.

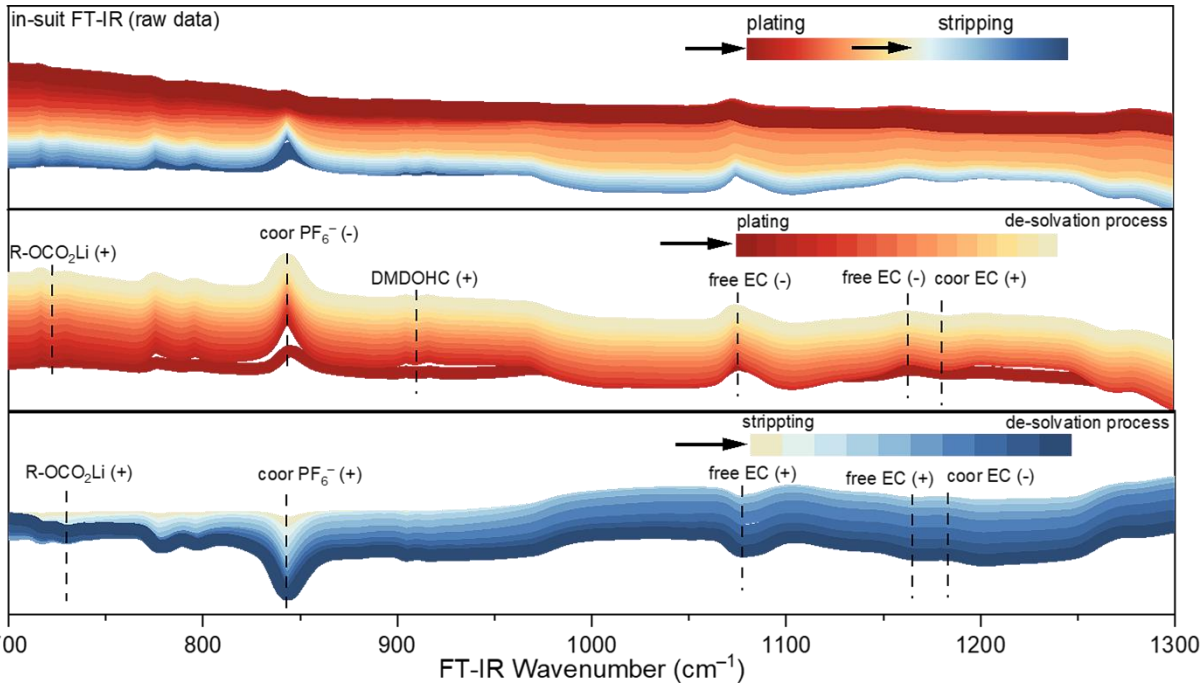

148

149 **Figure S19.** Contour plots of Fourier-transform infrared (FTIR) spectra of the

150 electrode/electrolyte interfaces in a 1 M $LiPF_6$ EC/DMC.

151 As far as in situ IR spectroscopy is concerned, additional Li^+ is required for the lithium

152 deposition phase of Li||Cu cell, so that the undissociated lithium salts in the electrolyte

153 dissociate, and then the Li^+ combines with the free solvent to form a new solvated structure.

154 The peaks correspond to 842.9 cm^{-1} for coor PF_6^-, 1074.3 cm^{-1} and 1161.1 cm^{-1} for free EC,

155 1278.8 cm^{-1} for free DMC, 1184.3 cm^{-1} for coor EC, and 1305.8 cm^{-1} for coor DMC, as shown

156 in Figure 2h. However, the opposite occurs during the stripping process. Nevertheless, we

157 observed that the free EC and free DMC did not return to their initial states due to the

158 irreversible decomposition of electrons gained at the interface to form different types of lithium

159 alkyls (R-OCO_2Li at 715.6 cm^{-1} and HCOOLi at 775.4 cm^{-1}) as well as solvent-derived ester

160 organics (DMDOHC at 910.4 cm^{-1}).

161

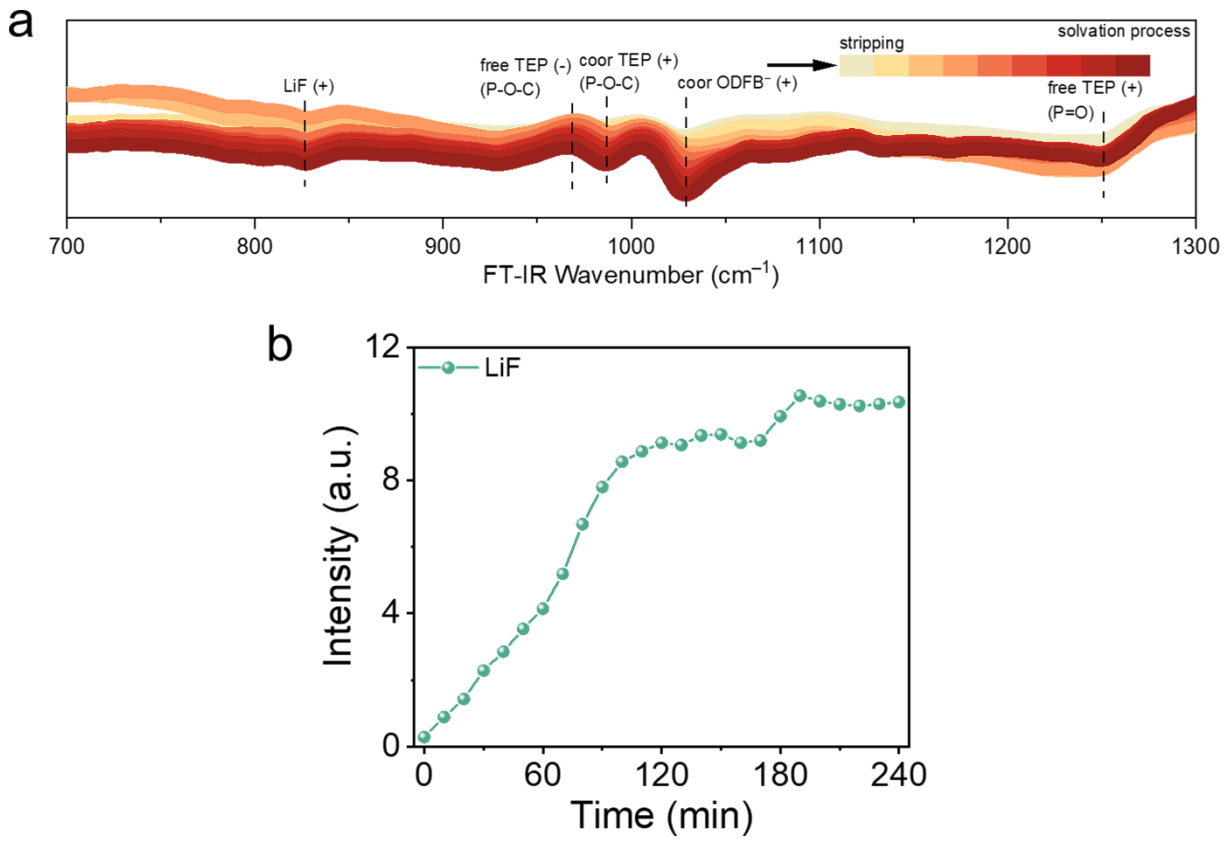

Figure S20. (a) Contour plots of Fourier-transform infrared (FTIR) spectra of the electrode/electrolyte interfaces in a 0.5 M-DBN. (b) LiF content variation in in situ FTIR.

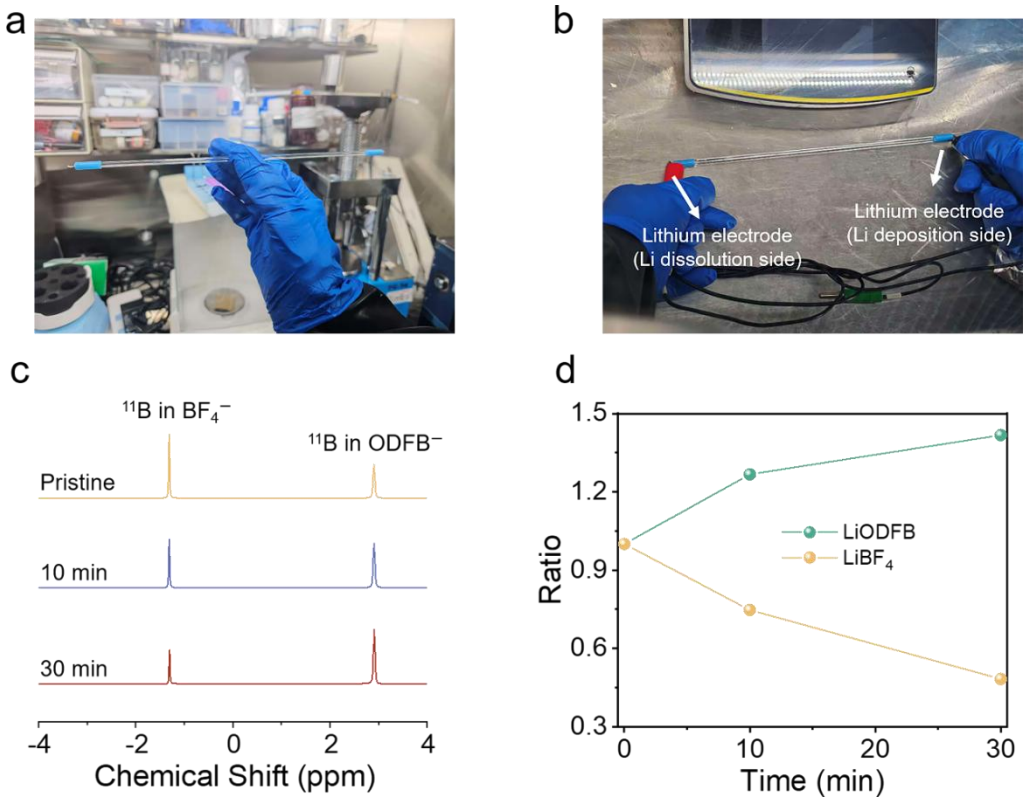

Figure S21. (a, b) Experimental setup for ion migration studies using 0.5 M-DBN electrolyte. (c) Quantitative NMR results showing the electrolyte composition near the lithium deposition electrode. (d) Relative compositional changes in the electrolyte near the lithium deposition electrode.

We employed quantitative nuclear magnetic resonance (NMR) spectroscopy to examine the concentration changes of two lithium salts near the anode side during the charging process. Specifically, a Li–Li symmetric cell was assembled and subjected to a constant current of 0.2 mA. After approximately 10 and 30 minutes of current application, 0.3 mL of electrolyte was collected from the vicinity of the electrode and mixed with 0.3 mL of deuterated chloroform ($CDCl_3$). The resulting solution was analyzed using ^{11}B NMR spectroscopy, and the relative concentrations of the two anions were determined by integrating the corresponding peaks. Figures a and b show the schematic of the experimental setup. As illustrated in Figures c and d, with increasing lithium insertion time (simulating the charging process in a full cell), the concentration of the $ODFB^-$ anion near the lithium deposition electrode (anode side) gradually increased, while that of the BF_4^- anion decreased. This trend is consistent with the predictions from our molecular dynamics (MD) simulations.

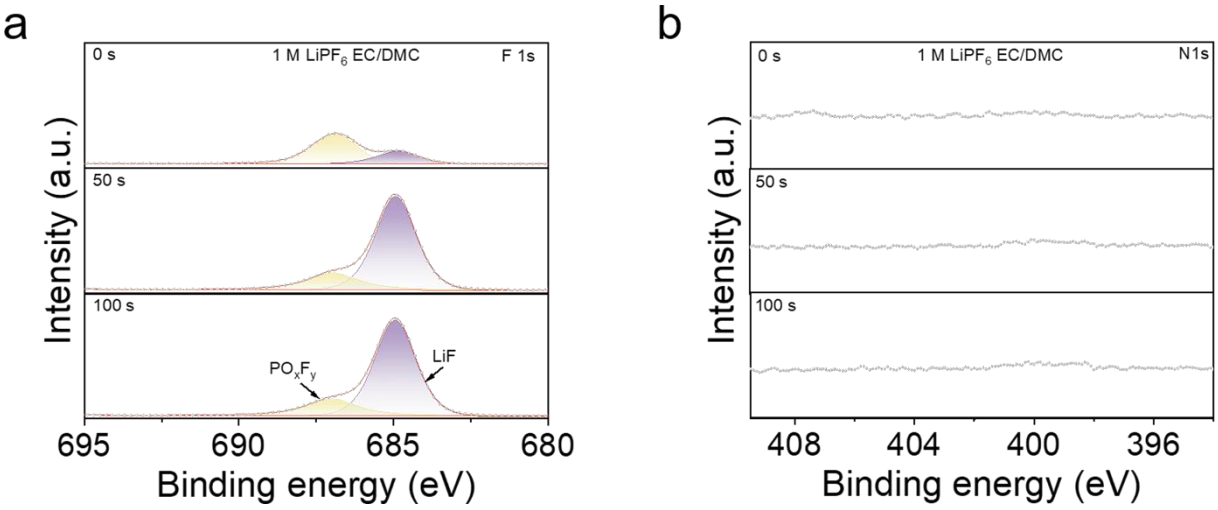

Figure S22. F1s (a) and N1s (b) XPS spectra of lithium metal anode in 1 M $LiPF_6$ EC/DMC electrolyte after different sputtering times (0 s, 50 s, 100 s).

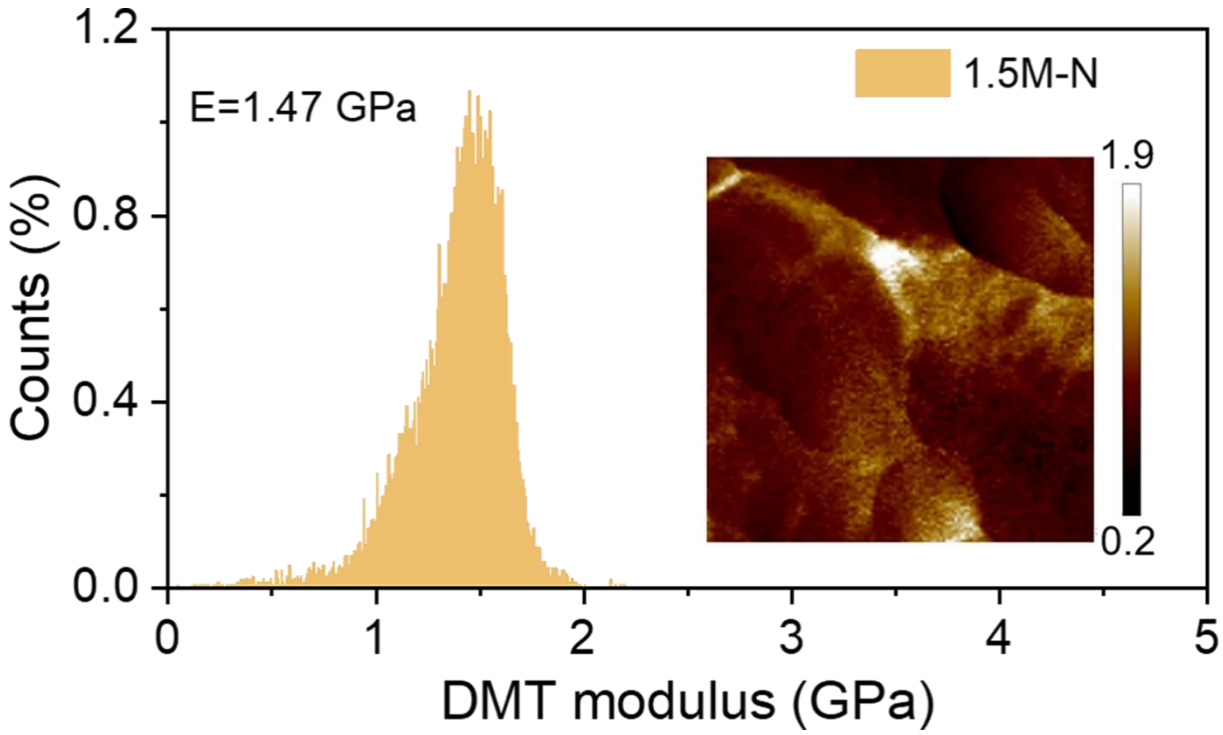

187

188 **Figure S23.** DMT modulus distribution of 1.5 M-N SEI.

189

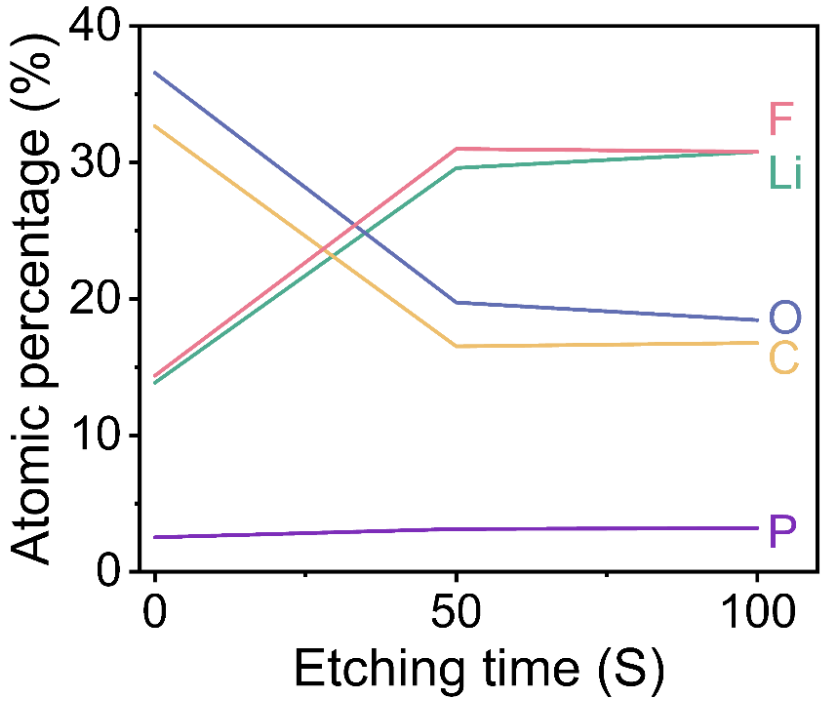

190

191 **Figure S24.** Atomic concentrations of SEIs formed at different depths in the 1M $LiPF_6$

192 EC/DMC electrolyte.

193

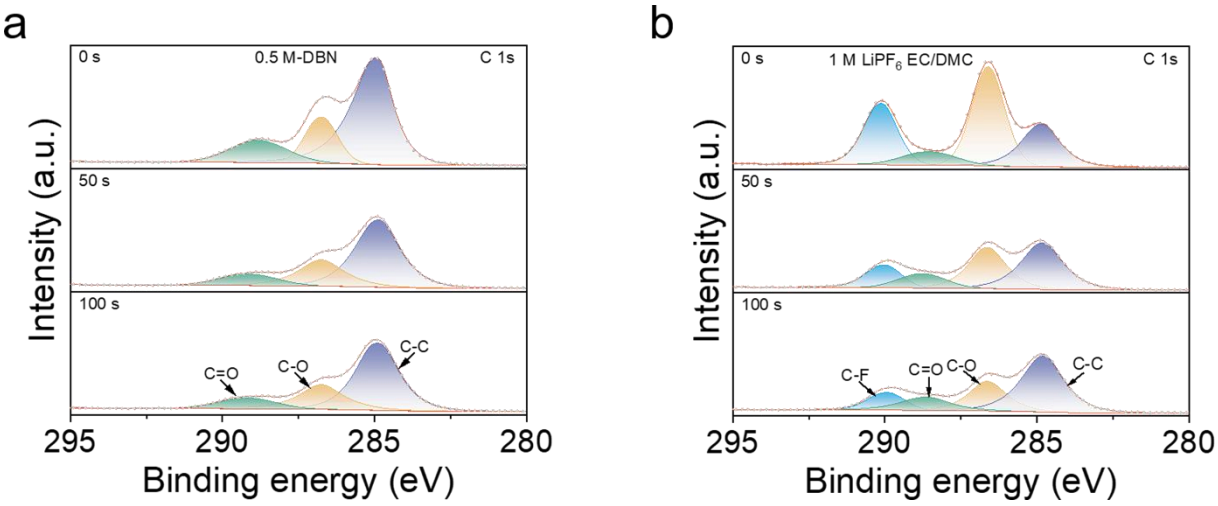

194

195 **Figure S25.** C1s XPS spectra of LMA in 0.5 M-DBN (a) and 1 M $LiPF_6$ EC/DMC (b)

196 electrolytes after different sputtering times (0 s, 50 s, 100 s).

197

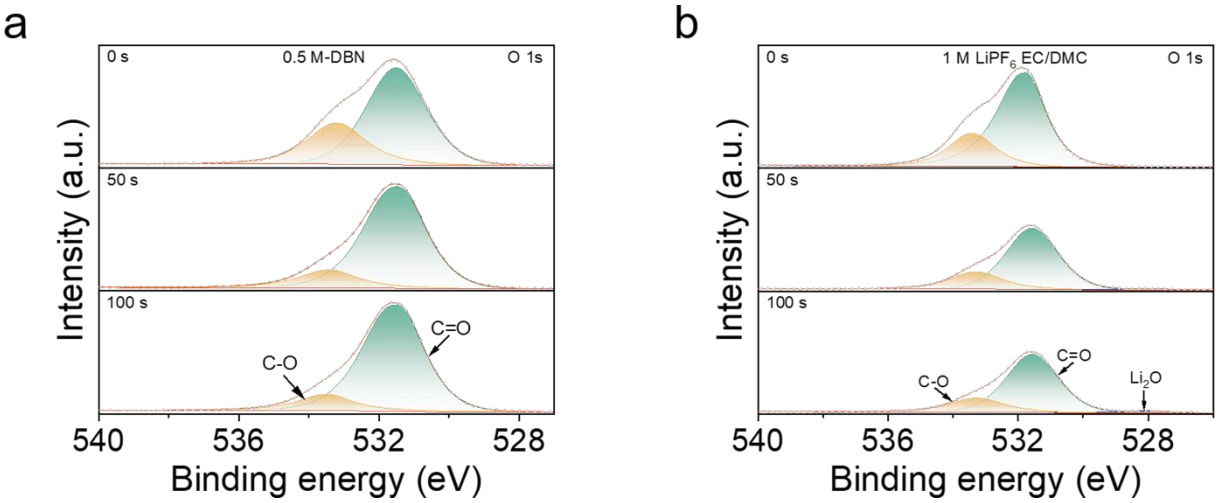

198

199 **Figure S26.** O1s XPS spectra of LMA in 0.5 M-DBN (a) and 1 M $LiPF_6$ EC/DMC (b)

200 electrolytes after different sputtering times (0 s, 50 s, 100 s).

201

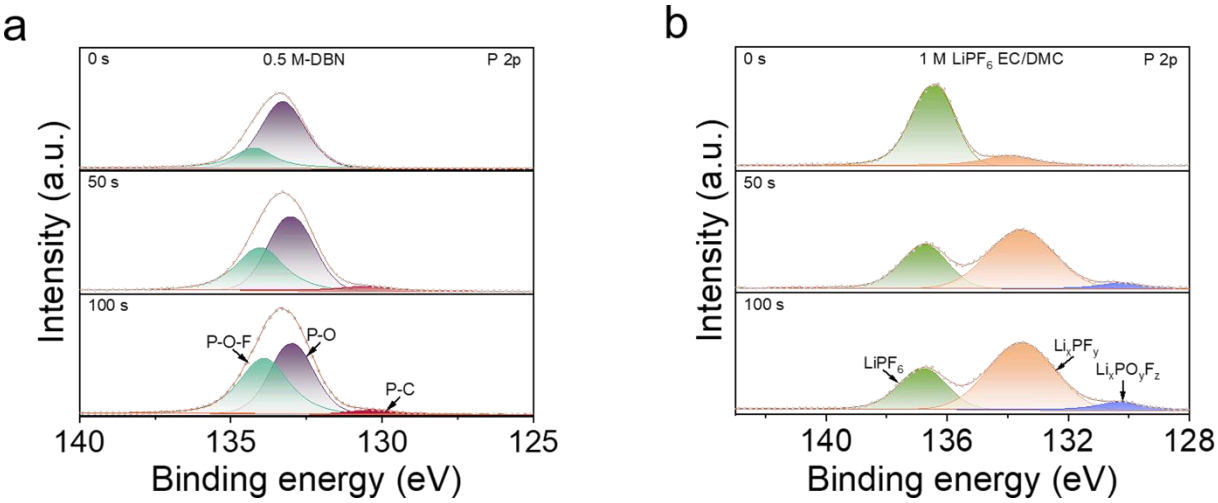

202

203 **Figure S27.** P2p XPS spectra of LMA in 0.5 M-DBN (a) and 1 M $LiPF_6$ EC/DMC (b)

204 electrolytes after different sputtering times (0 s, 50 s, 100 s).

205

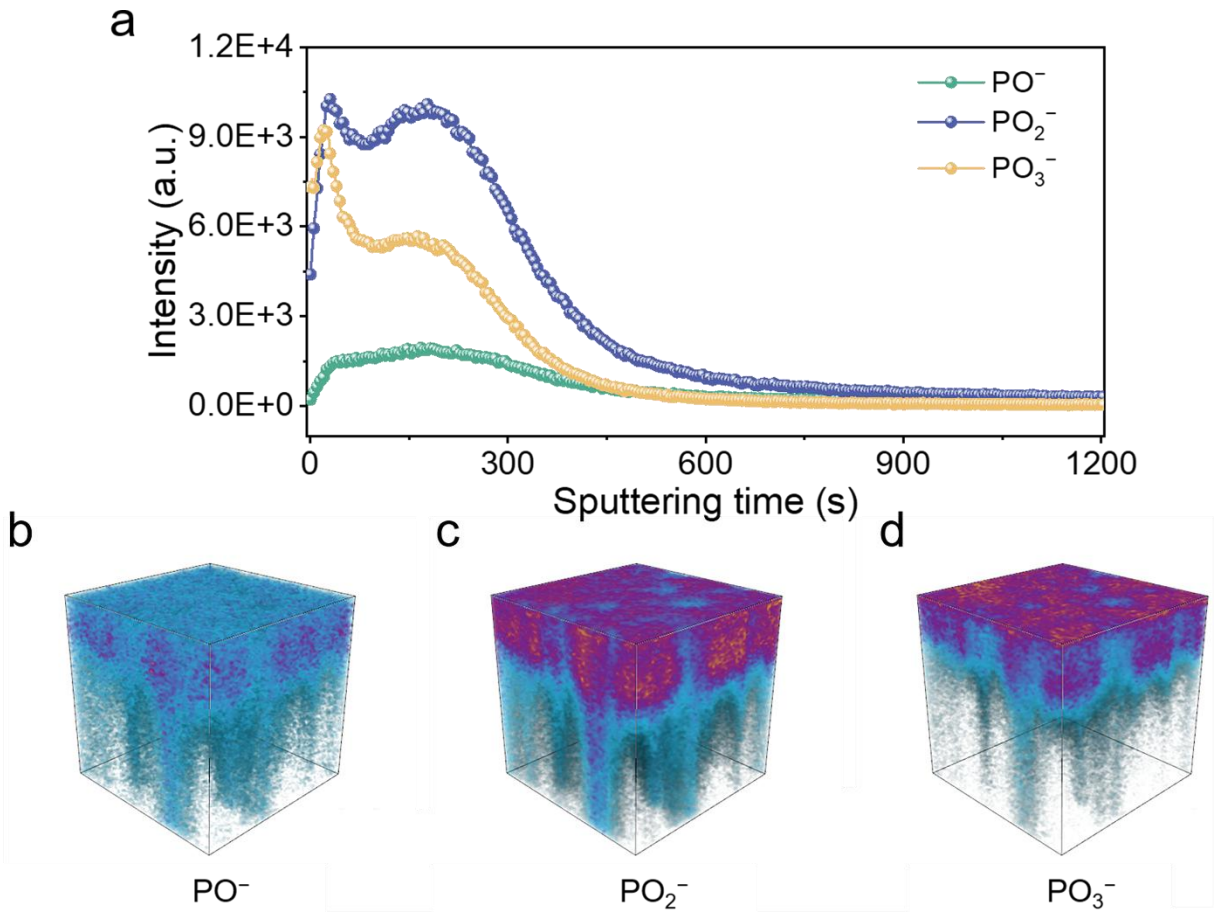

206

207 **Figure S28.** Time-of-flight secondary ion mass spectrometry (TOF-SIMS) depth distributions

208 (a-c) and three-dimensional images of various species (d) within a 0.5 M-DBN electrolyte.

209

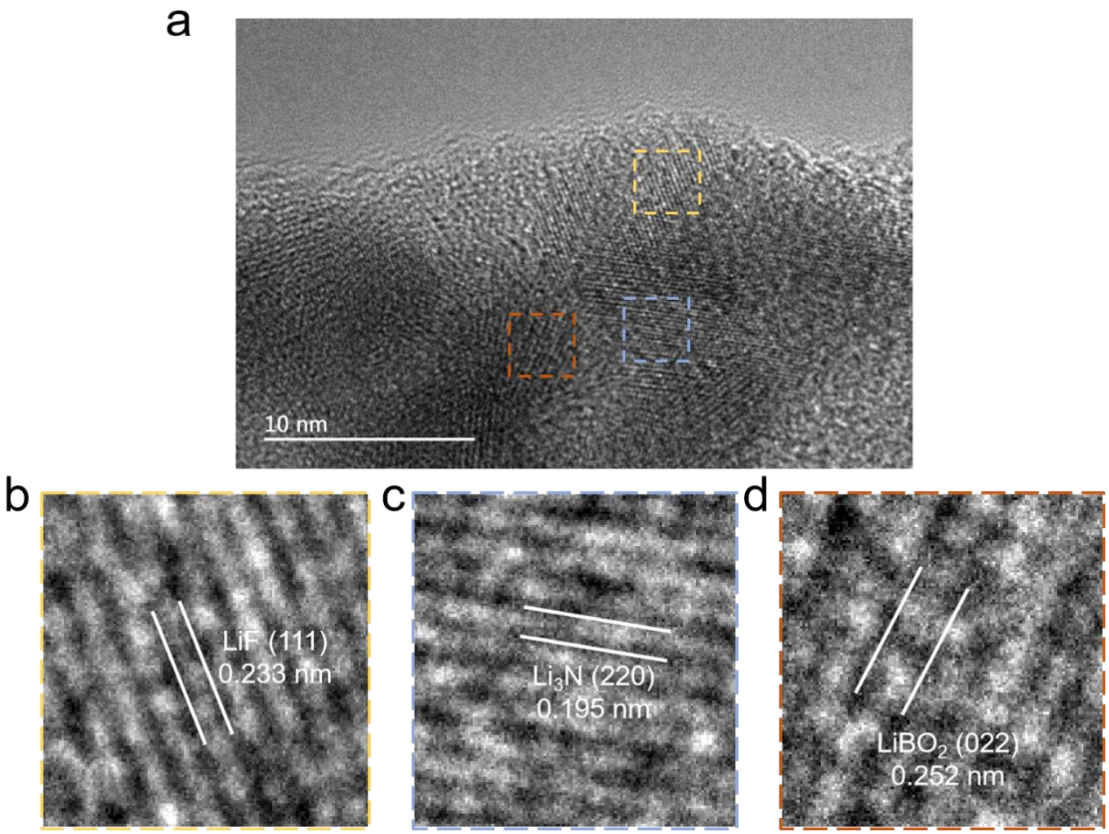

Figure S29. (a) Cryo-TEM image of the SEI formed on lithium metal using the 0.5 M-DBN electrolyte; the colored rectangles indicate the presence of LiF (yellow), Li_3N (blue), and $LiBO_2$ (maroon). The marked regions in the cryo-TEM image (a) are enlarged in (b–d), showing the corresponding nanocrystals of LiF (b), Li_3N (c), and $LiBO_2$ (d), each exhibiting distinct lattice fringes.

As shown in Figure S27a, the SEI layer formed using the 0.5 M-DBN electrolyte exhibits a dense, inorganic-rich morphology on the lithium metal surface. High-resolution analysis identified several crystalline components within the SEI, including the LiF (111) plane with a lattice spacing of 0.233 nm, the Li_3N (220) plane (0.195 nm), and the $LiBO_2$ (022) plane (0.252 nm), as displayed in Figures S27b–d. These observations reveal a distinct layered structure: the inner SEI region is primarily composed of Li_3N and $LiBO_2$, while the outer layer is dominated by LiF. This spatial distribution is fully consistent with our earlier XPS depth profiling and TOF-SIMS results. Such a stratified SEI structure offers synergistic advantages: the outer LiF layer provides high interfacial rigidity that effectively suppresses lithium dendrite growth, whereas inner compounds like Li_3N exhibit high Li^+ conductivity, enhancing ionic transport through the SEI. Additionally, the presence of B–O bonded components contributes to mechanical flexibility. Together, these features enable the formation of a robust SEI with both high ionic conductivity and mechanical adaptability, facilitating dense lithium deposition and significantly improving plating/stripping efficiency.

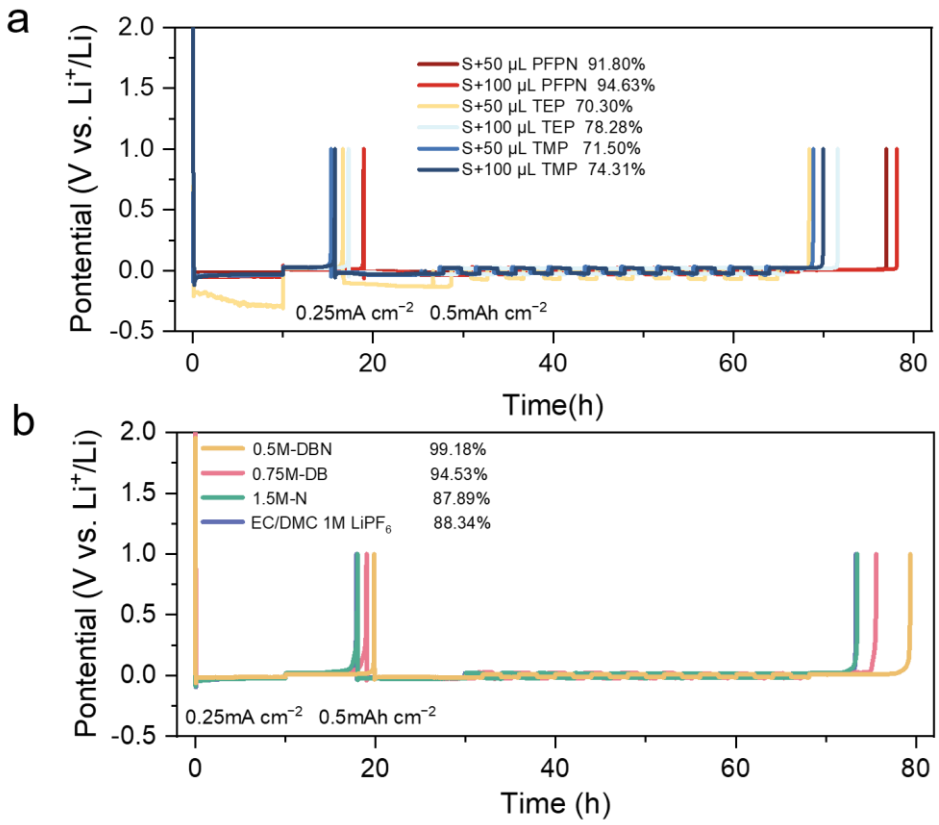

Figure S30. (a) CE of commercial electrolytes containing TMP, TEP, and PFPN additives measured by the Aurbach method. (b) CE was determined by a modified Aurbach method at 25 °C and 0.25 mA cm^{-2} current density.

Three commonly used flame retardants (TMP, TEP, and PFPN) were individually added to a commercial electrolyte (1 M $LiPF_6$ in EC/DMC, denoted as S) in volumes of 50 μL and 100 μL. Their Coulombic efficiencies (CE) were evaluated using the Aurbach method. The results showed that the S + 100 μL TEP system exhibited the highest CE among the flame-retardant-modified electrolytes, reaching 94.63%, which is an improvement over the baseline commercial electrolyte (88.34%) (Figure S27a). However, this value still falls short of the CE achieved by the 0.5 M-DBN electrolyte (99.18%) (Figure S27b). The superior performance of the 0.5 M-DBN system is primarily attributed to the synergistic decomposition of the three lithium salts, which forms a highly stable triphasic interphase with enhanced interfacial stability and Li^+ transport properties.

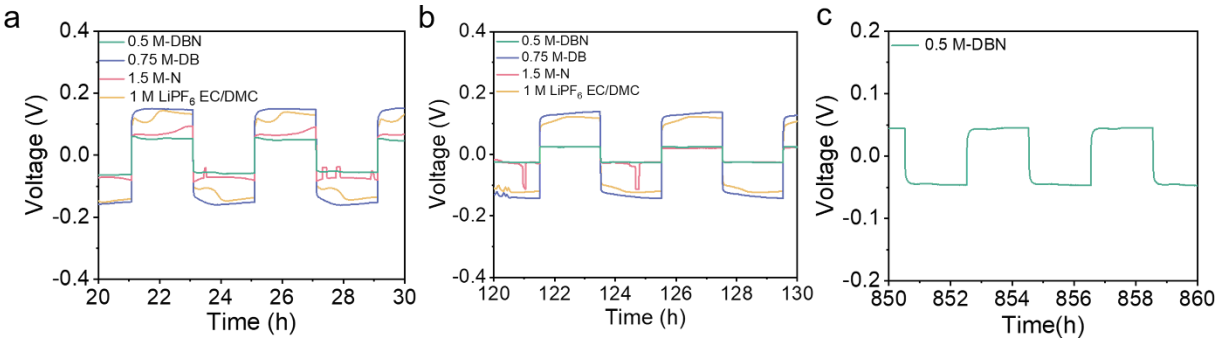

Figure S31. Corresponding amplification voltage-time curves for Li-Li symmetric cells in 0.5 M-DBN, 0.75 M-DB, 1.5 M-N, and 1 M $LiPF_6$ EC/DMC electrolytes at a current density of 0.5 mA cm^{-2} and a capacity of 1 mAh cm^{-2}. Time intervals: 20-30 hours (a), 120-130 hours (b) and 850-860 hours (c).

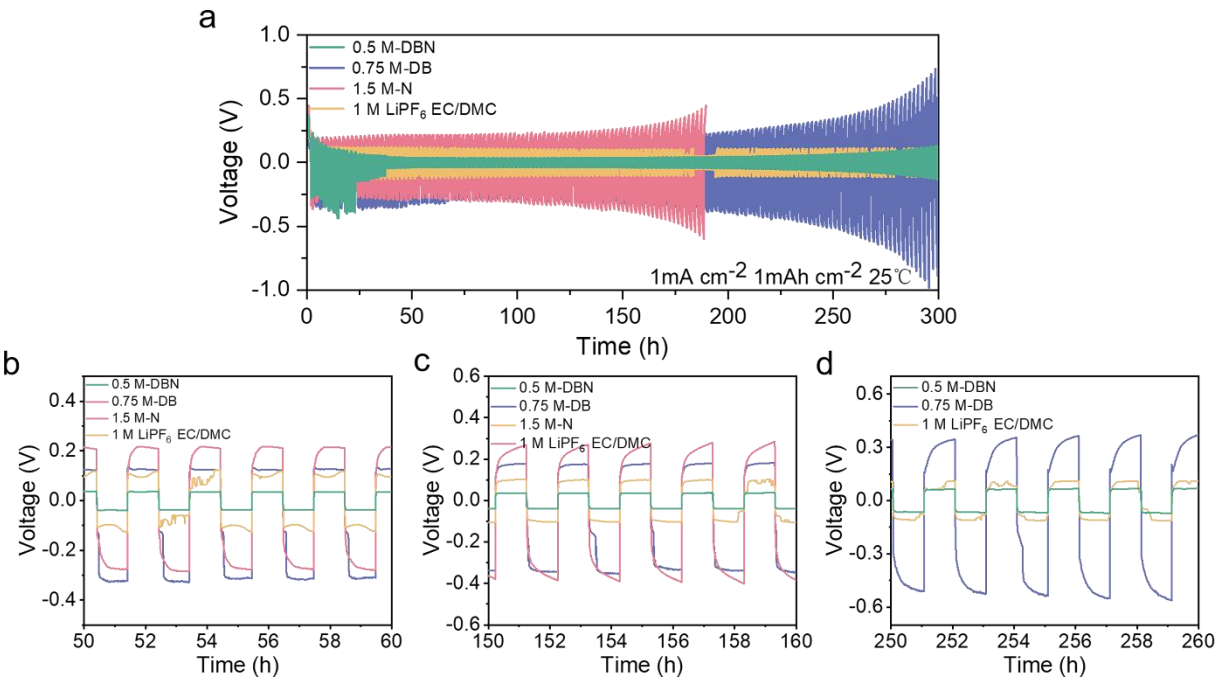

Figure S32. (a) Voltage-time curves of Li/Li symmetric cells in 0.5 M-DBN,0.75 M-DB,1.5 M-N, and 1 M $LiPF_6$ EC/DMC electrolytes at a current density of 1 mA cm^{-2} and a capacity of 1 mAh cm^{-2}; corresponding amplified voltage-time curves of Li/Li symmetric cells. Time intervals: 50-60 hours (b), 150-160 hours (c), and 250-260 hours (d).

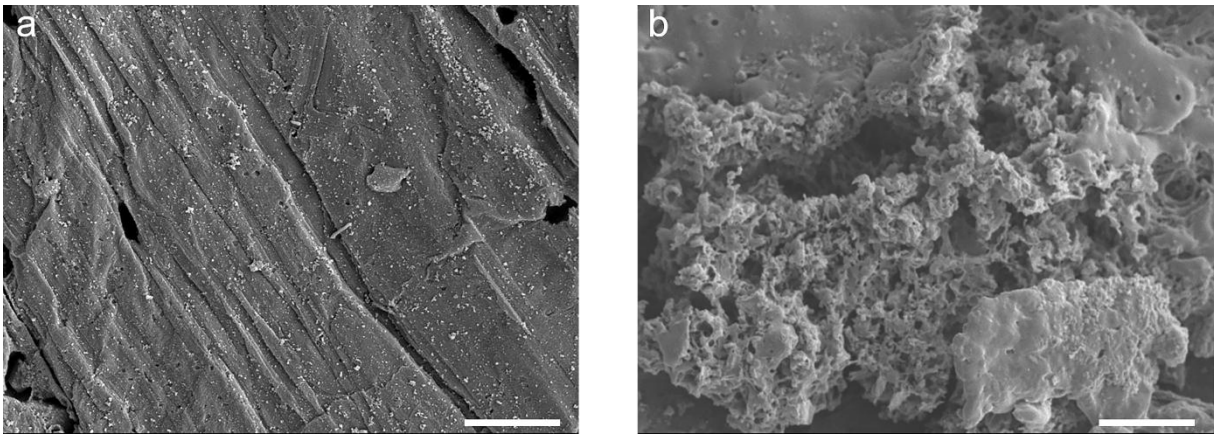

Figure S33. SEM images of lithium metal anode cycled in 0.5 M-DBN (a) and 1 M $LiPF_6$ EC/DMC (b) electrolytes. Scale bar: 10 μm (a, b).

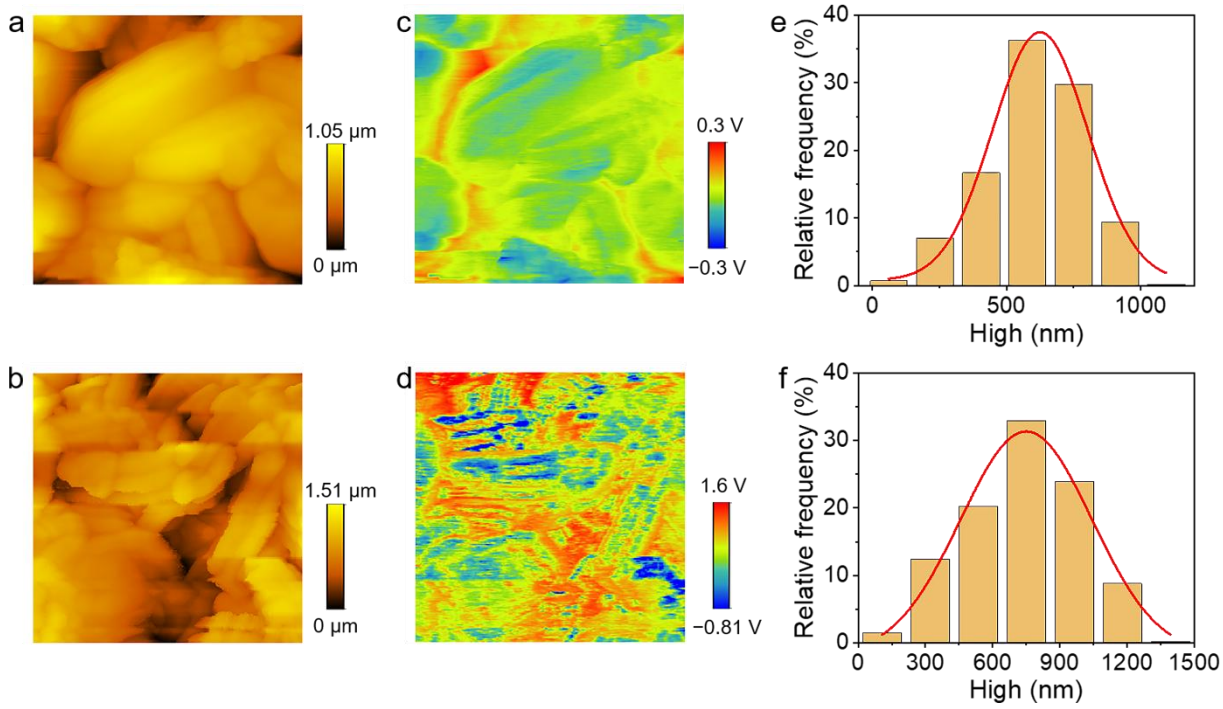

261

262 **Figure S34.** Surface morphology (a, b) and surface potential maps (c, d) of lithium metal plated

263 on copper foil in 0.5 M-DBN (a, c, e) and 1 M $LiPF_6$ EC/DMC (b, d, f) electrolytes and their

264 normal distribution of surface morphology (e, f).

265

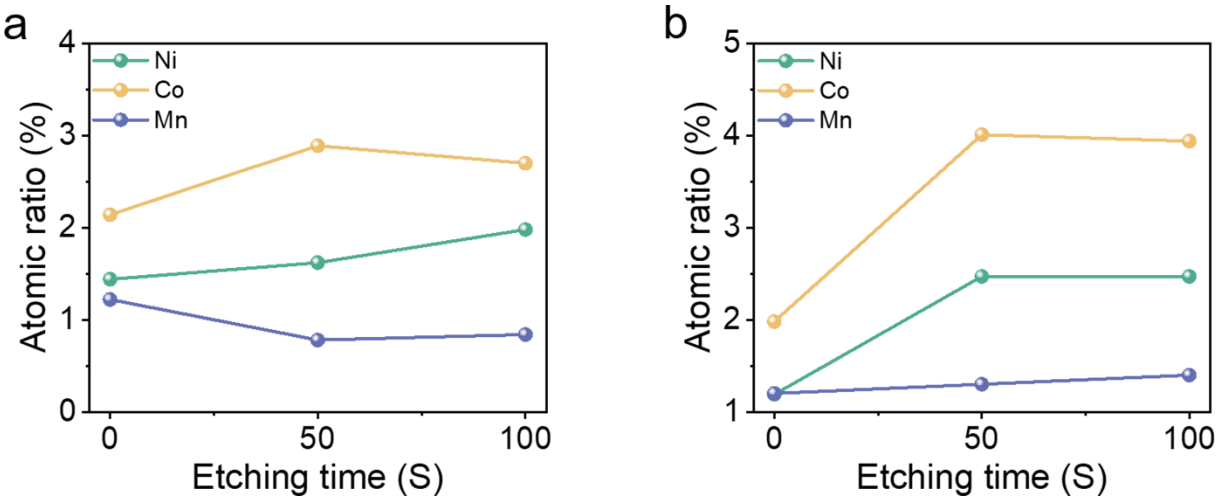

Figure S35. Atomic ratios of Ni, Co, and Mn at the lithium-metal interface for 0.5M-DBN (a) and 1 M $LiPF_6$ EC/DMC (b) at different sputtering times.

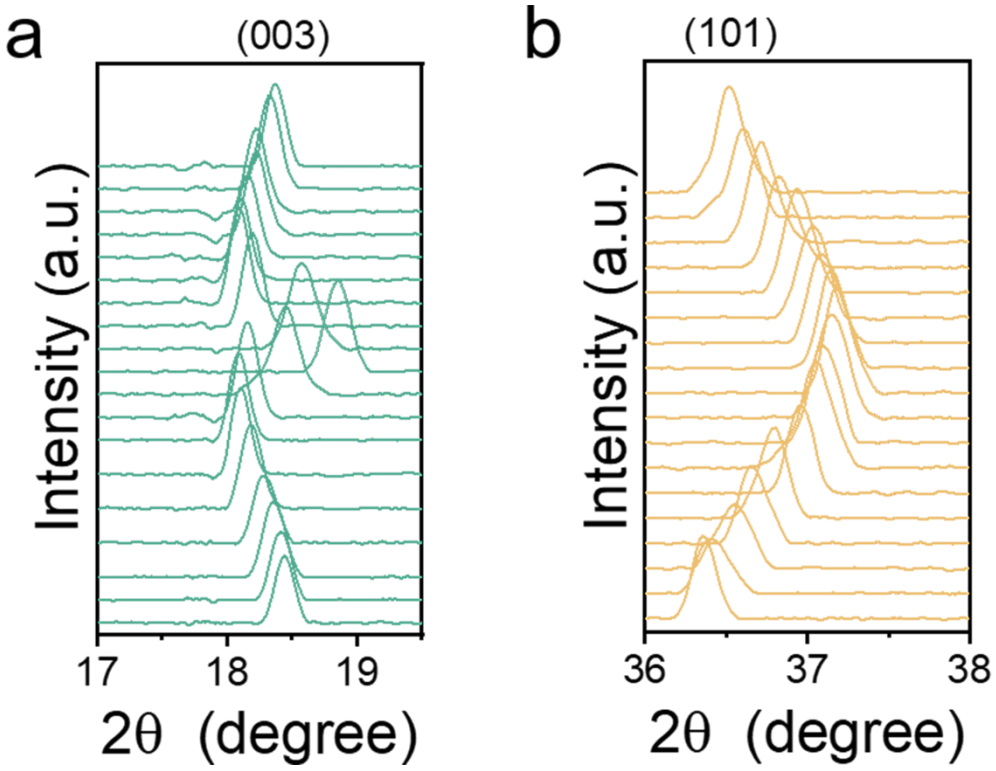

271

272 **Figure S36.** 003(a) and 101(b) crystal stacking diagrams of NCM811 cathodes of 1 M $LiPF_6$

273 EC/DMC electrolyte obtained by in situ XRD measurements (using laboratory facilities) during

274 charging and discharging at 0.5C.

275

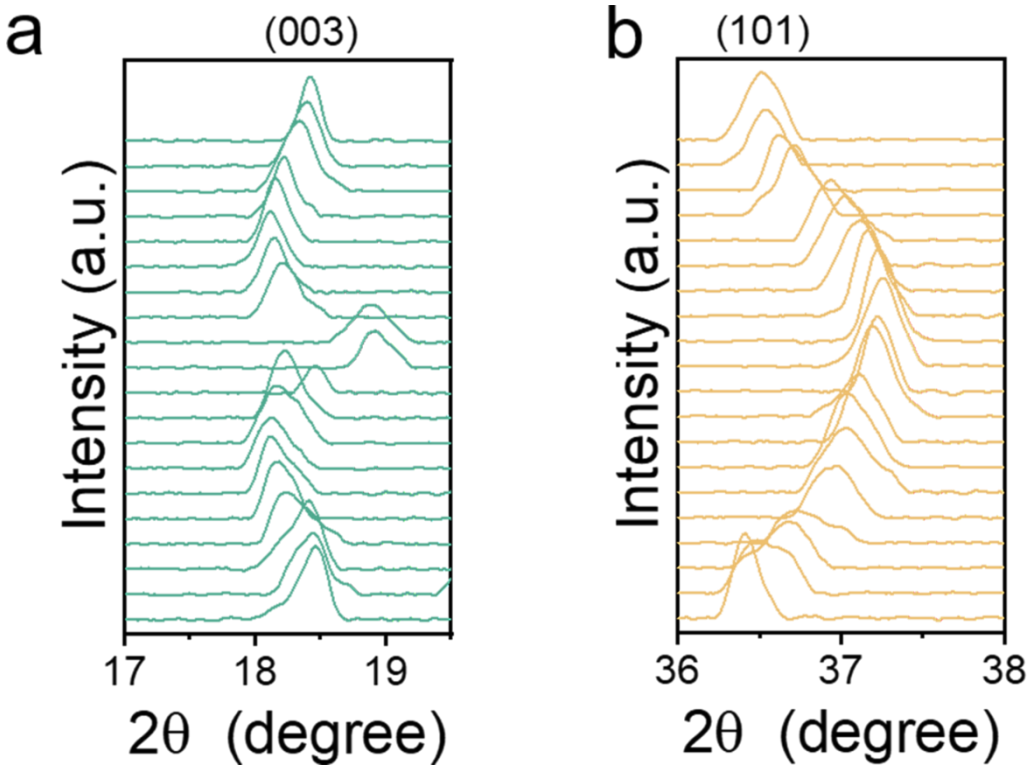

276

277 **Figure S37.** 003(a) and 101(b) crystal stacking diagrams of NCM811 cathodes of 0.5 M-DBN

278 electrolyte obtained by in situ XRD measurements (using laboratory facilities) during charging

279 and discharging at 0.5 C.

280

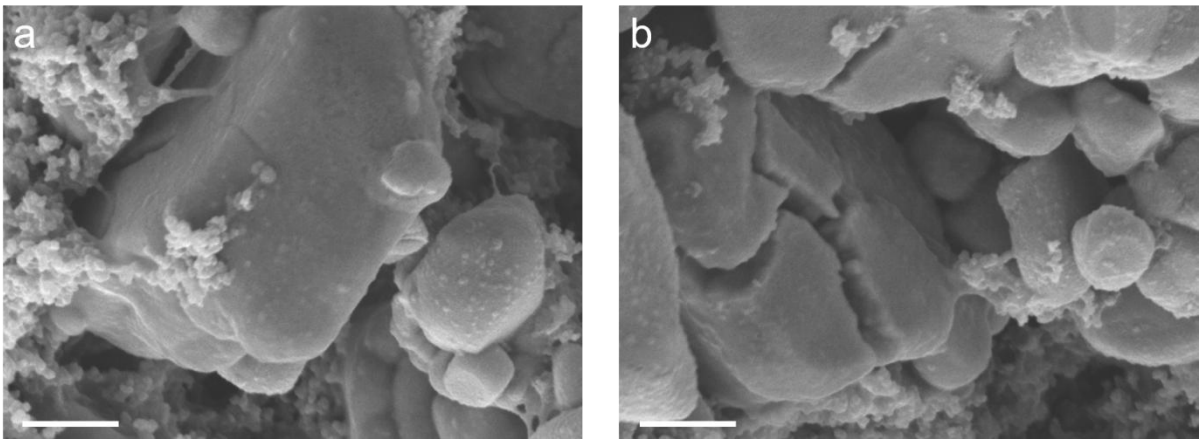

Figure S38. SEM images of cross-sectional NCM811 cathodes cycled in 0.5 M-DBN (a) and 1 M $LiPF_6$ EC/DMC (b) electrolytes. Scale bar: 1 um (a, b).

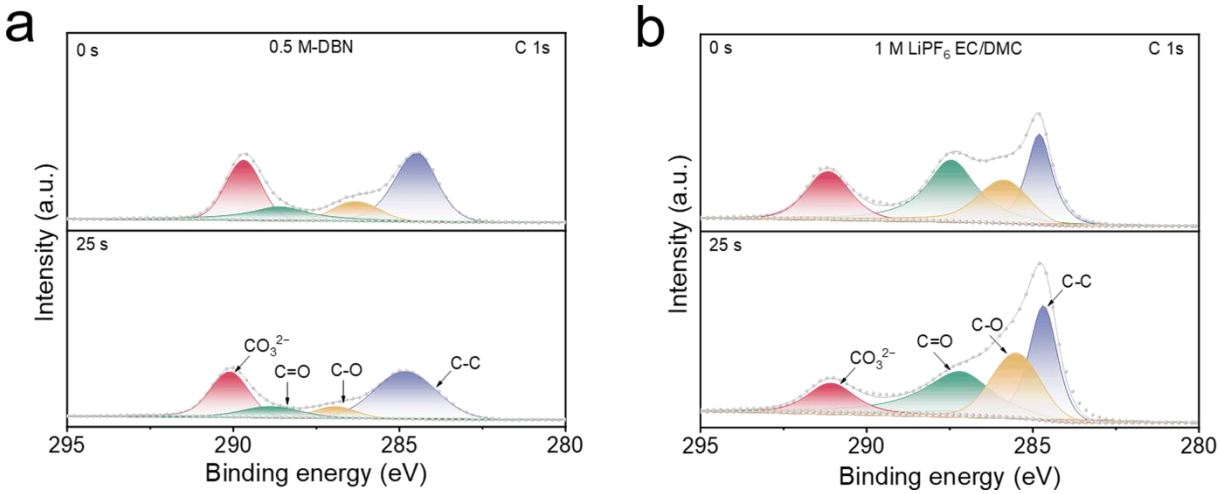

Figure S39. C1s XPS spectra of NCM811 cathode in 0.5 M-DBN (a) and 1 M $LiPF_6$ EC/DMC (b) electrolytes after different sputtering times (0 s, 25 s).

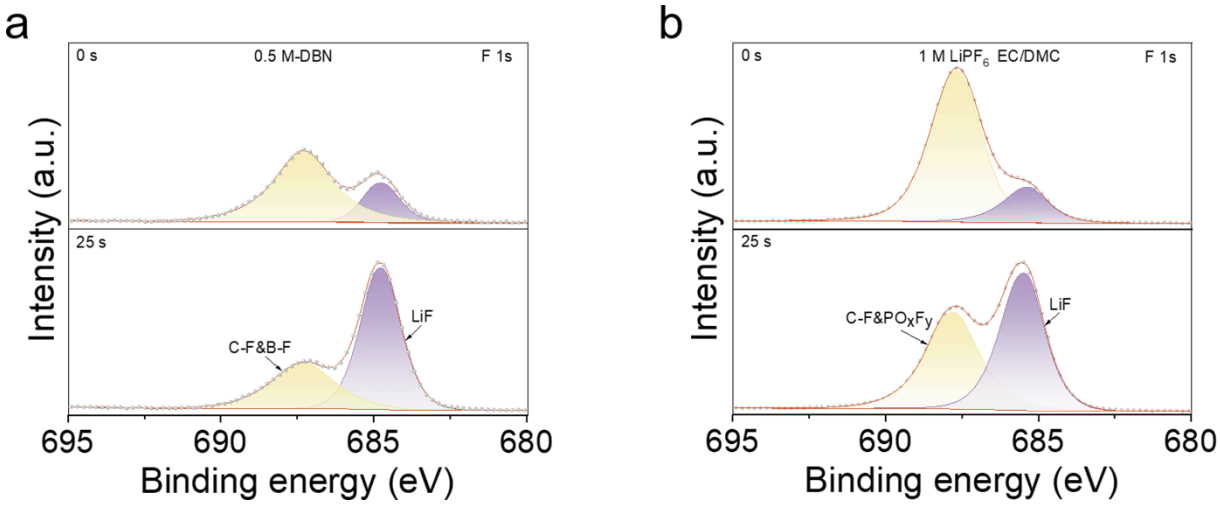

289

290 **Figure S40.** F1s XPS spectra of NCM811 cathode in 0.5 M-DBN (a) and 1 M $LiPF_6$ EC/DMC

291 (b) electrolytes after different sputtering times (0 s, 25 s).

292

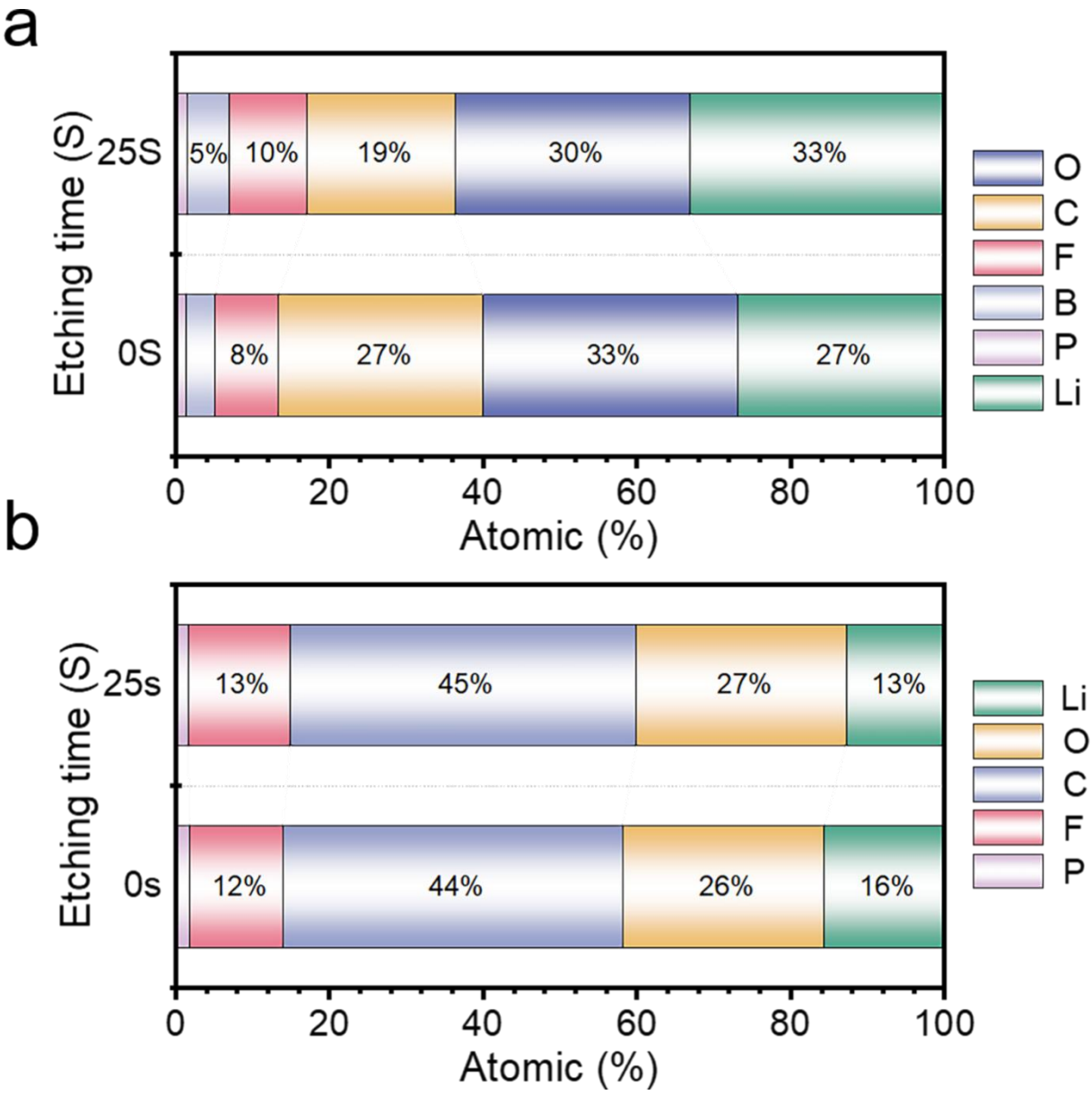

Figure S41. SEI information obtained by quantifying the atomic ratios of different elements was measured using XPS on NCM811 cathodes in 0.5 M-DBN (a) and 1 M $LiPF_6$ EC/DMC (b) electrolytes.

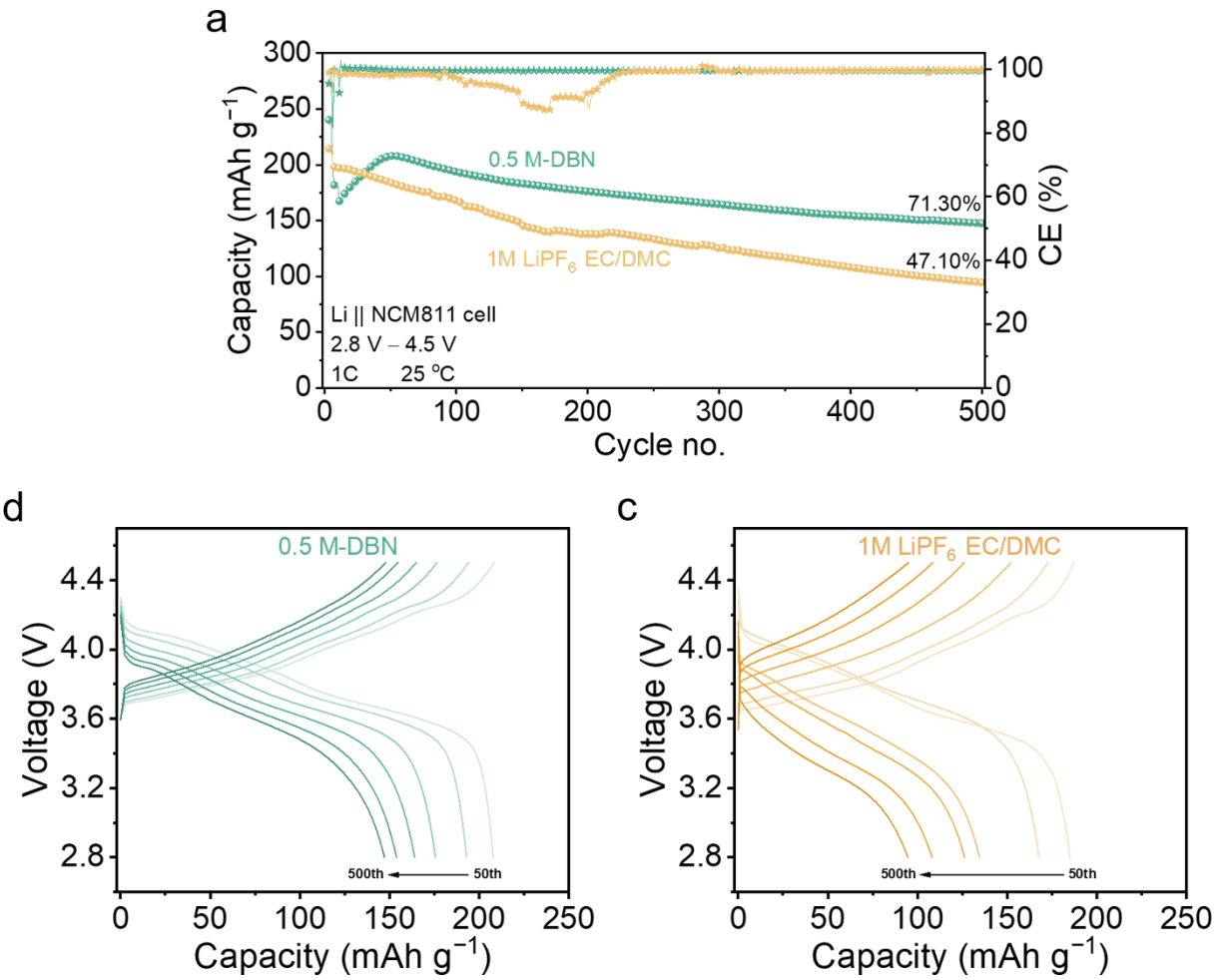

298

299 **Figure S42.** (a) Cycling performance and CE of NCM 811 cathode in 0.5 M-DBN and 1 M

300 $LiPF_6$ EC/DMC electrolytes at 0.2 A g^{-1} multiplicity with up to 4.5 V. Corresponding voltage

301 profiles of cell using (b) 0.5 M-DBN and (c) 1 M $LiPF_6$ EC/DMC electrolyte.

302

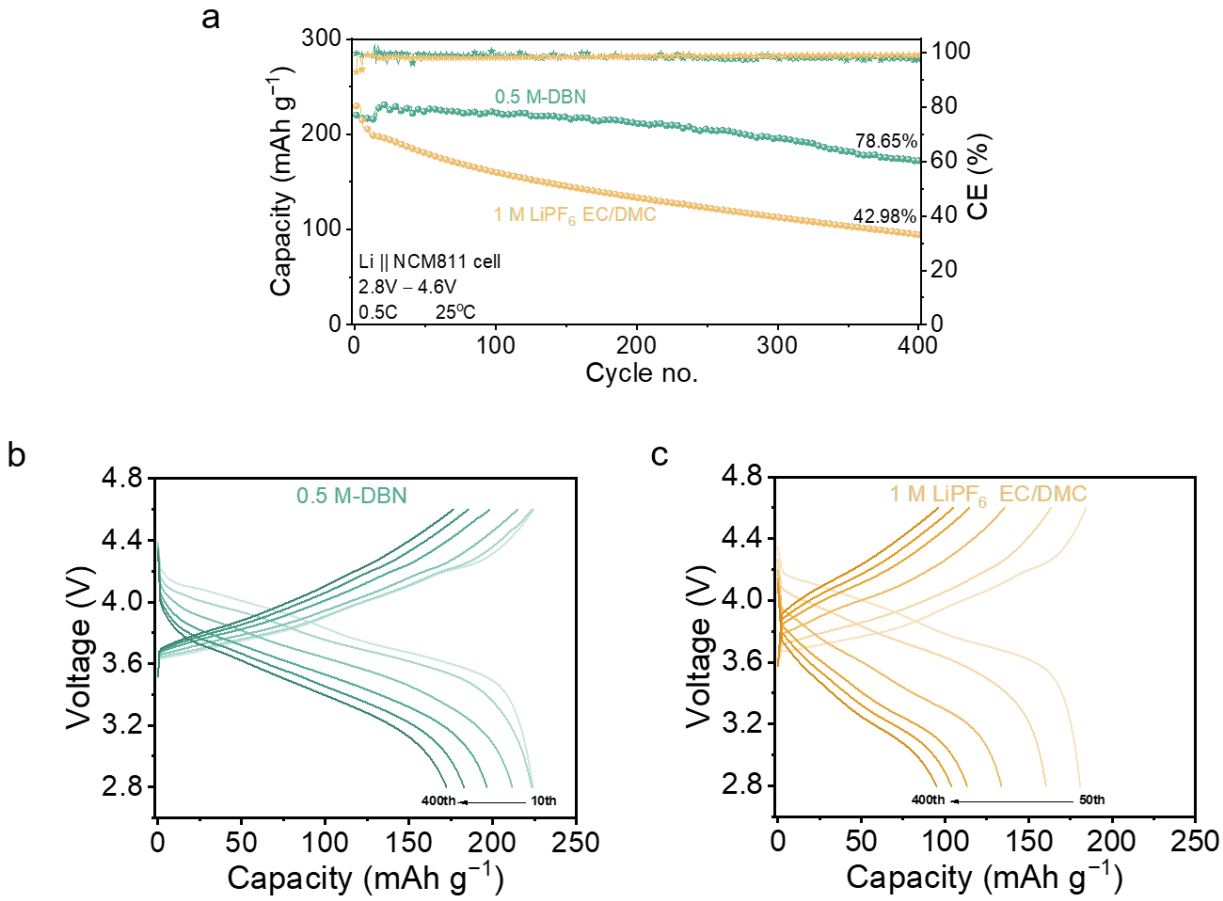

303

304 **Figure S43.** (a) Cycling performance and CE of NCM811 cathode in 0.5 M-DBN and 1 M

305 $LiPF_6$ EC/DMC electrolytes at 0.1 A g^{-1} multiplicity with up to 4.6 V. Corresponding voltage

306 profiles of cell using (b) 0.5 M-DBN and (c) 1 M $LiPF_6$ EC/DMC electrolyte.

307

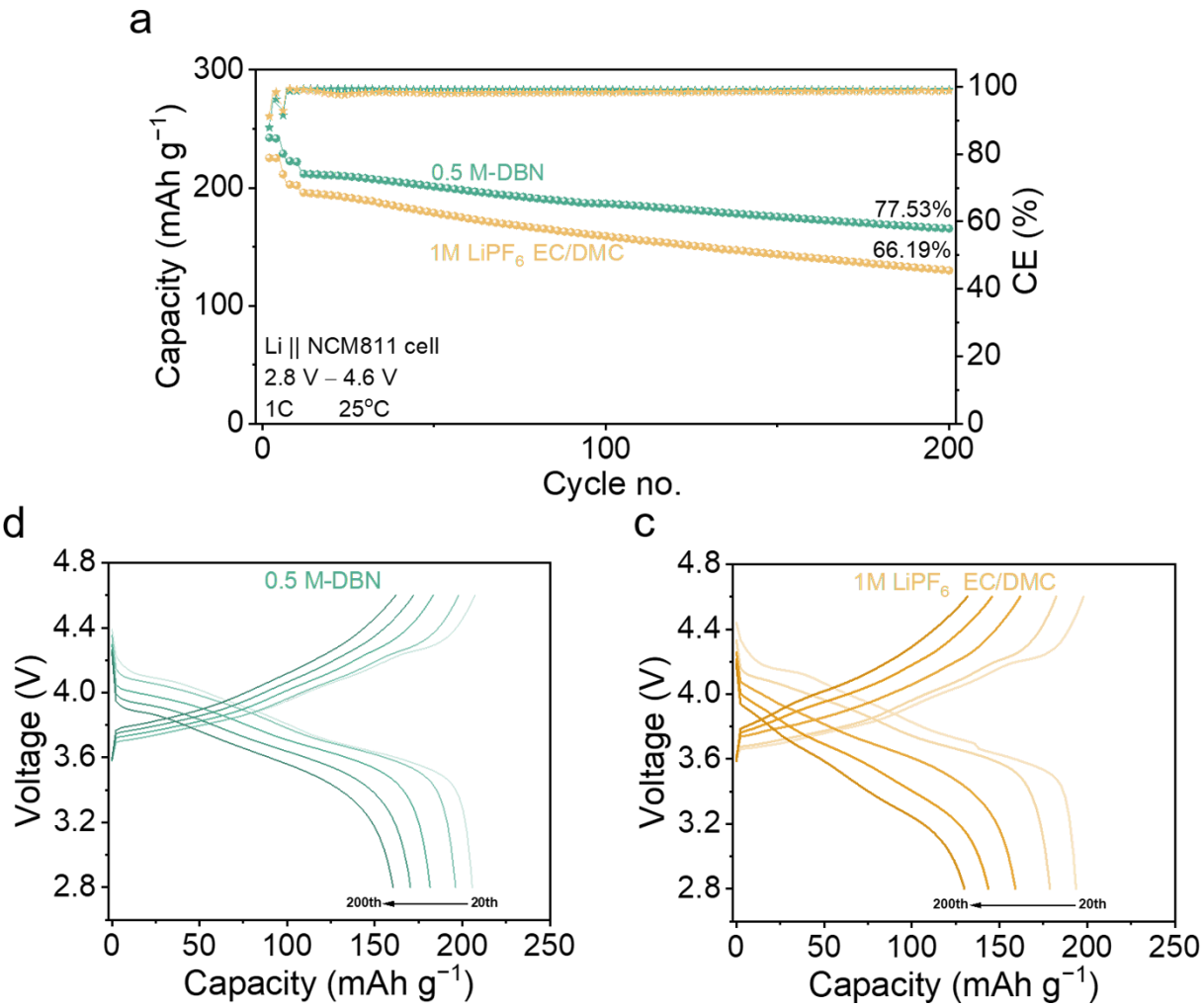

Figure S44. (a) Cycling performance and CE of NCM 811 cathode in 0.5 M-DBN and 1 M $LiPF_6$ EC/DMC electrolytes at 0.2 A g^{-1} multiplicity with up to 4.6 V. Corresponding voltage profiles of cell using (b) 0.5 M-DBN and (c) 1 M $LiPF_6$ EC/DMC electrolyte.

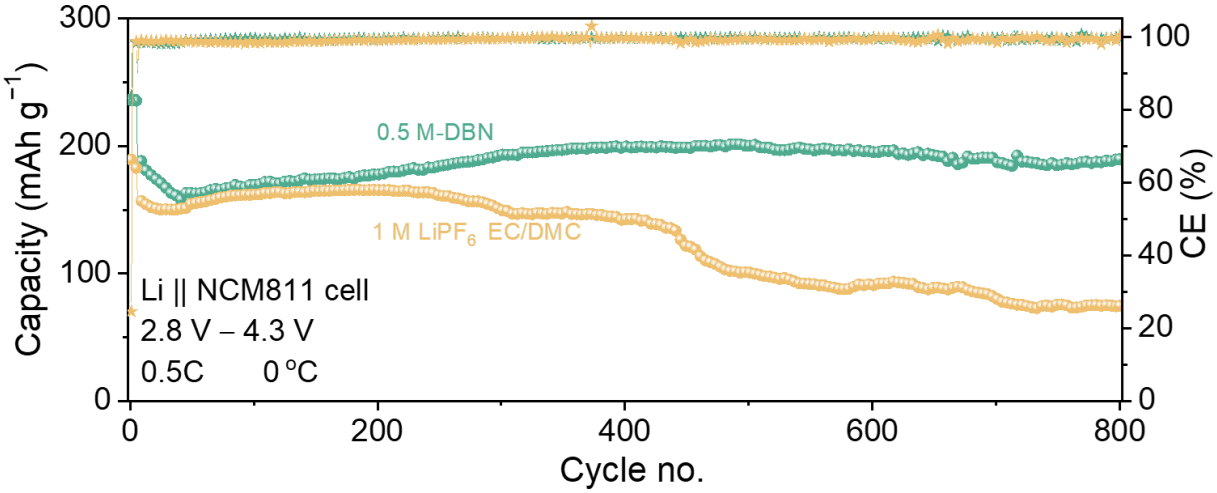

313

314 **Figure S45.** Electrochemical performance of NCM811 cathode using 0.5 M-DBN and 1 M

315 $LiPF_6$ EC/DMC electrolyte voltage range of 2.8 V-4.3 V at 0 °C.

316

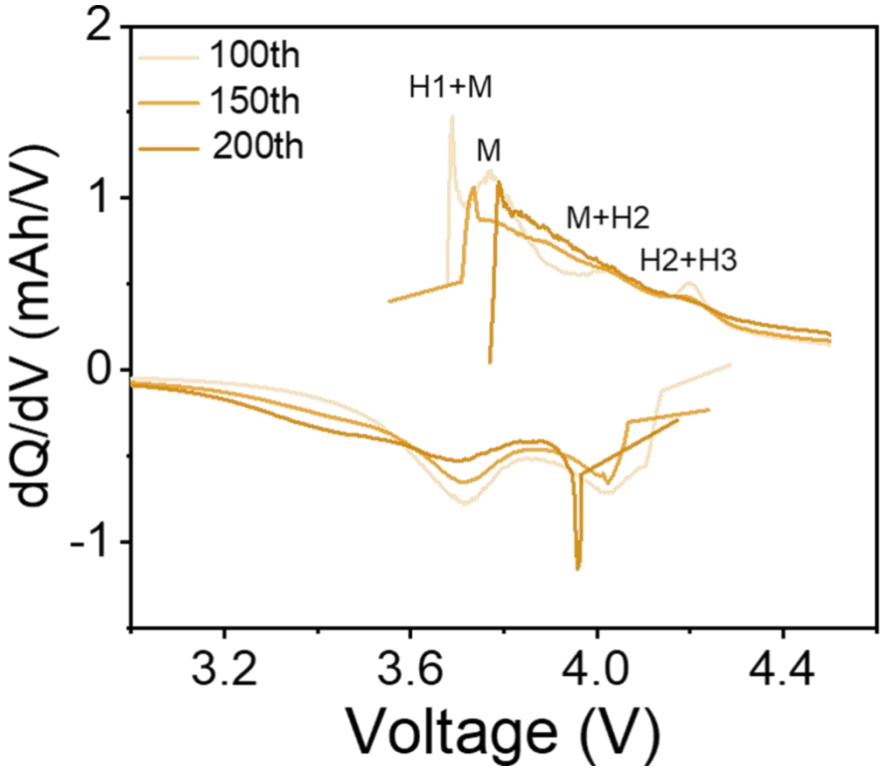

317

318 **Figure S46.** dQ/dV curves of NCM 811 cathode using 1 M $LiPF_6$ EC/DMC electrolyte at 0.1

319 A g^{-1} multiplication with a cutoff voltage of 4.5 V.

320

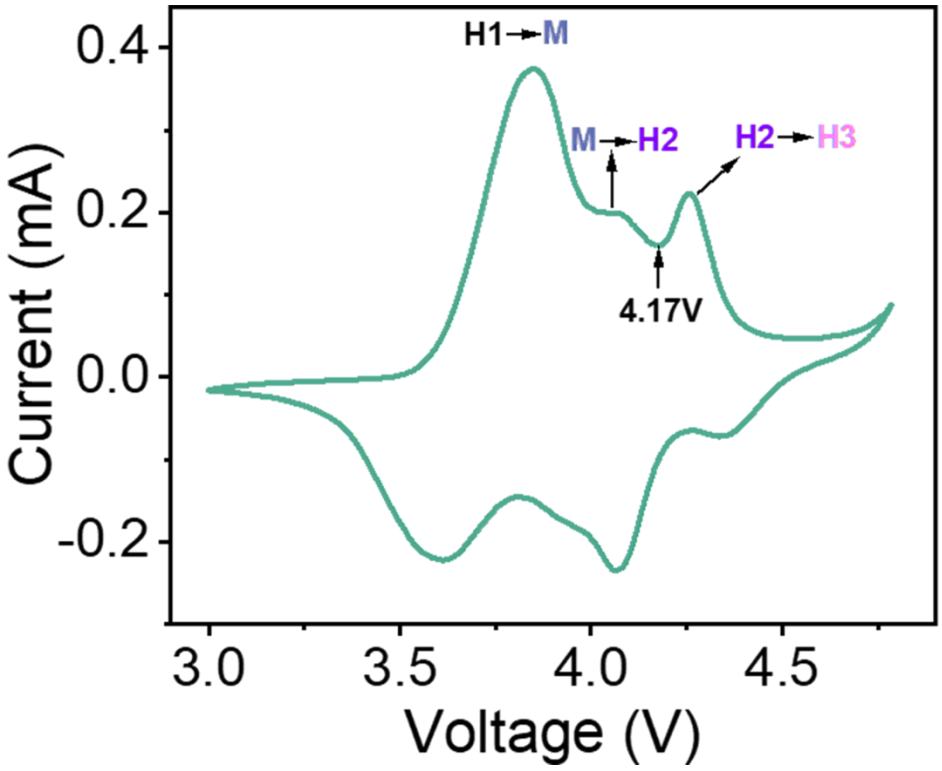

Figure S47. Typical cyclic voltammetry (CV) curve of NCM 811 cathode in 0.5 M-DBN electrolyte at a scan rate of 0.1 mV s^{-1}.

The CV curve of the NCM811 cathode typically shows a four-step phase transition from hexagonal (H1) to monoclinic (M) to hexagonal (H2 and H3). The H1→M transition is split into two overlapping peaks above 4.15 V due to the involvement of $Co^{4+/3+}$ redox pairs in the redox process. The H2→H3 transition in the NCM811 cathode is inevitably accompanied by oxidation of lattice oxygen, resulting in significant unit cell volume change and secondary particle cracking. This transition and the oxidative reduction of lattice oxygen are the main reasons for the decrease in capacity and reversibility of NCM811.

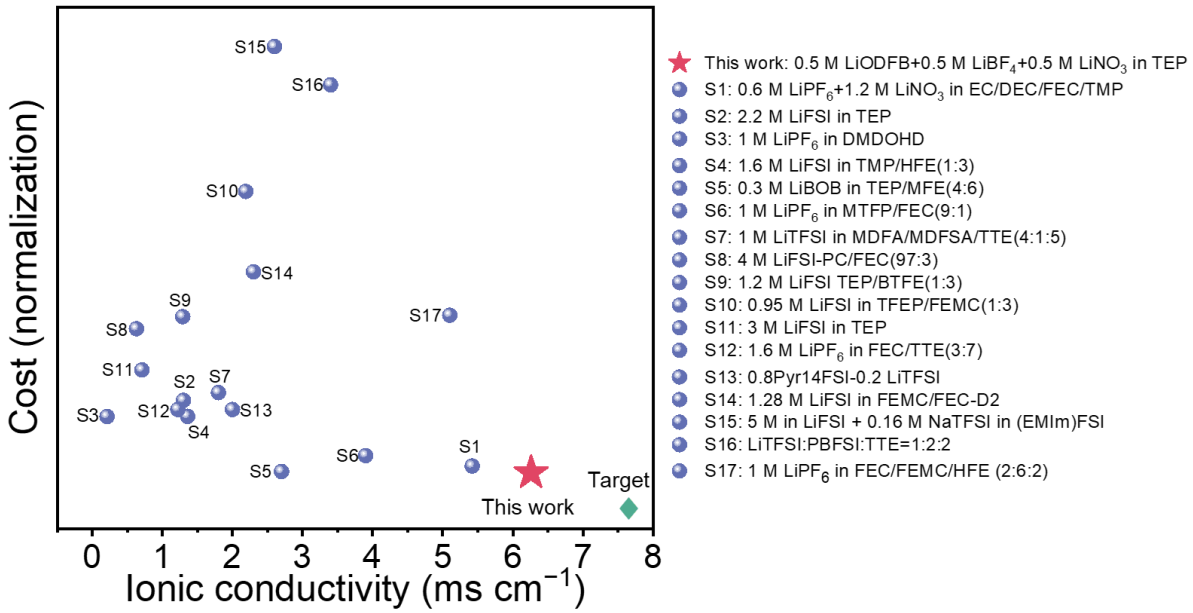

Figure S48. Summary comparison of ionic conductivity and cost of state-of-the-art nonflammable electrolytes.

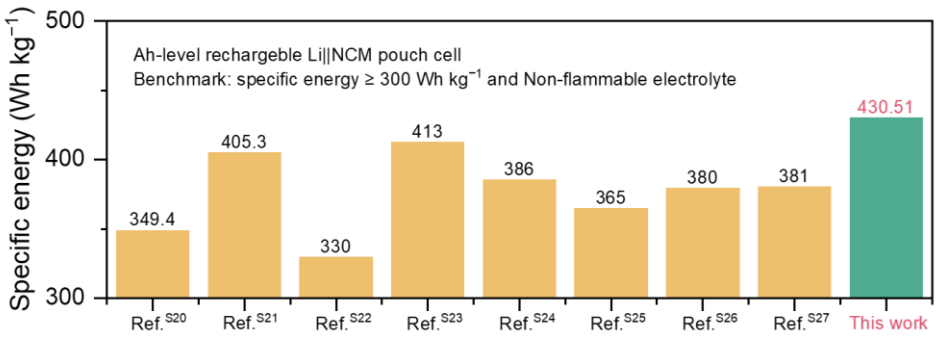

336

337 **Figure S49.** In both published literature and this work, lithium metal pouch cells with high

338 energy density and non-flammable electrolytes exhibit state of the art performance.

339

340 **Table S1.** Detailed components of the four MD models

Components	TEP	LiODFB	$LiBF_4$	$LiNO_3$
0.5 M LiODFB+0.5 M $LiBF_4$ +0.5 M $LiNO_3$ in TEP (mmol)	5.9	0.5	0.5	0.5
Molecule number	589.0	50.0	50.0	50.0

341

342

343

344 **Table S2.** LiF and Li_3N strengths and ionic conductivity

Species	Strength of SEI （GPa）	Ionic conductivity of SEI ($S\ cm^{-1}$)
LiF	64.97	10^{-9}~10^{-14}
Li_3N	＞50.00	2-4×10^{-4}

345

346

347 **Table S3.** Prices of salts and solvents used in the preparation of electrolytes for lithium batteries.

Chemical	Full name	CAS No.	Price per unit ($)
$LiPF_6$	Lithium hexafluorophosphate	21324-40-3	8.4 g^{-1}
LiTFSI	Lithium bis(trifluoromethanesulfonyl)imide	90076-65-6	3.84 g^{-1}
$LiBF_4$	Lithium tetrafluoroborate	14283-07-9	12.96 g^{-1}
LiODFB	Lithium difluoro(oxalato)borate	409071-16-5	9.6 g^{-1}
LiFSI	Lithium bis(fluorosulfonyl)imide	171611-11-3	23.4 g^{-1}
LiBOB	Lithium bis(oxalato)borate	244761-29-3	1.86 g^{-1}
$LiNO_3$	Lithium nitrate	7790-69-4	0.175 g^{-1}
NaTFSI	Sodium Bis(Trifluoromethanesulfonyl)Imide	91742-21-1	101.83 g^{-1}
EC	Ethylene carbonate	96-49-1	0.131 g^{-1}
DMC	Dimethyl carbonate	616-38-6	3.386 g^{-1}
DEC	Diethyl Carbonate	105-58-8	0.307 g^{-1}
PC	Propylene carbonate	108-32-7	0.134 g^{-1}
FEC	Fluoroethylene carbonate	114435-02-8	8.07 g^{-1}
HFE	1,1,2,2-Tetrafluoroethyl-2′,2′,2′-trifluoroethyl ether	406-78-0	0.78 g^{-1}
DMDOHD	Dimethyl 2,5-Dioxahexanedioate	88754-66-9	5.36 g^{-1}
MFE	Methyl Perfluorobutyl Ether	163702-07-6	1.27 g^{-1}
MTFP	Methyl 3,3,3-trifluoropionate	13089-11-7	0.71 g^{-1}
MDFA	Methyl Difluoroacetate	433-53-4	10.16 g^{-1}
MDFSA	Methyl Difluoro(fluorosulfonyl)acetate	680-15-9	13.67 g^{-1}
TTE	1,1,2,2-Tetrafluoroethyl-2,2,3,3-tetrafluoropropyl ether	16627-68-2	2.95 g^{-1}
BTFE	Bis(2,2,2-trifluoroethyl) ether	333-36-8	13.4 g^{-1}
FEMC	3,3,3-Fluoroethylmethyl carbonate	167951-80-6	17 g^{-1}
Pyr14FSI	1-Butyl-1-methylpyrrolidinium Bis(fluorosulfonyl)imide	1057745-51-3	33 g^{-1}
TEP	Triethyl phosphate	78-40-0	0.134 g^{-1}
TMP	Trimethyl phosphate	512-56-1	0.225 g^{-1}
(EMIm)FSI	3-Ethyl-1-Methyl-1H-Imidazol-3-Ium Bis(Fluorosulfonyl)Amide	235789-75-0	16.3 g^{-1}

348

349

Table S4. Summary of assessed costs of the latest non-flammable electrolytes for lithium batteries

Electrolyte	Ionic conductivity (ms cm^{-1})	Reference	Evaluated Cost ($ L^{-1})
1.0.5 M LiODFB+0.5 M $LiBF_4$+0.5 M $LiNO_3$ in TEP	4.13	This work	1452
2.0.6 M $LiPF_6$+1.2 M $LiNO_3$ in EC/DEC/FEC/TMP	5.42	S1	2228
3.2.2 M LiFSI in TEP	1.3	S2	9774
4.1 M $LiPF_6$ in DMDOHD	0.21	S3	7923
5.1.6 M LiFSI in TMP/HFE(1:3)	1.36	S4	7939
6.0.3 M LiBOB in TEP/MFE(4:6)	2.7	S5	1599
7.1 M $LiPF_6$ in MTFP/FEC(9:1)	3.9	S6	3427
8.1 M LiTFSI in MDFA/MDFSA/TTE(4:1:5)	1.8	S7	10671
9.4 M LiFSI-PC/FEC(97:3)	0.63	S8	18012
10.1.2 M LiFSI TEP/BTFE(1:3)	1.29	S9	19398
11.0.95 M LiFSI in TFEP/FEMC(1:3)	2.19	S10	33792
12.3 M LiFSI in TEP	0.71	S11	13274
13.1.6 M $LiPF_6$ in FEC/TTE(3:7)	1.22	S12	8728
14.0.8Pyr14FSI-0.2 LiTFSI	2	S13	8721
15.1.28 M LiFSI in FEMC/FEC-D2	2.3	S14	24557
16.5 M in LiFSI + 0.16 M NaTFSI in (EMIm)FSI	2.6	S15	50450
17. LiTFSI:PBFSI:TTE=1:2:2	3.4	S16	46045
18.1 M $LiPF_6$ in FEC/FEMC/HFE (2:6:2)	5.1	S17	19563

Table S5. Pouch cell energy density calculation

	Parameter	Value
Cathode (NCM811 with Al current collector)	Discharge Capacity	221 mAh g^{-1}
	Area weight	22 mg cm^{-2}
	Active material ratio	97%
	Area capacity	4.86 mAh cm^{-2}
	Number of layers	8
	Weight	15.13 g
Li anode	Li thickness	50 μm
	Number of layers	9
	Weight	1.92 g
Collector (Cu)	Cu thickness	8 μm
	Weight	1.93 g
Electrolyte	E/C ratio	1.75 g Ah^{-1}
	Weight	5.25
Separator	type	Polyethylene
	Weight	0.5 g
Package and tabs	Weight	1.75 g
	Size	7 cm*10 cm
Pouch cell	Discharge capacity	3 Ah
	Average voltage	3.8 V
	Weight	26.48 g
	Energy density	430.51 Wh kg^{-1}

Specific energy = discharge energy (Wh) / total weight (kg). This is a more precise calculation method compared to the method: Specific energy=discharge capacity (Ah) × mid-value voltage (V) / total weight (kg).

Table S6. Lennard-Jones parameters[S18-S19]

atom	σ (nm)	ε (KJ/mol)	Charge (e)
Li^+			
Li^+	0.21645	0.0764793	0.80
BF_4^-			
B	0.35814	0.39748	0.6620
F	0.31181	0.25104	−0.3655
F	0.31181	0.25104	−0.3655
F	0.31181	0.25104	−0.3655
F	0.31181	0.25104	−0.3655
NO_3^-			
N	0.315	0.71128	0.6352
O	0.286	0.87864	−0.4784
O	0.286	0.87864	−0.4784
O	0.286	0.87864	−0.4784
$DFOB^-$			
C	0.39967	0.359824	0.6604
C	0.39967	0.359824	0.6604
O	0.296	0.87864	−0.5376
O	0.296	0.87864	−0.5376
OS	0.300	0.71128	−0.5950
OS	0.300	0.71128	−0.5950
B	0.364	0.75312	1.0392
F	0.312	0.255224	−0.4474
F	0.312	0.255224	−0.4474
TEP			
P	0.374	0.8368	2.1376
O	0.296	0.87864	−0.9188
O1	0.290	0.58576	−0.6499
O1	0.290	0.58576	−0.6803
O1	0.290	0.58576	−0.7062
C	0.350	0.276144	−0.0101
C	0.350	0.276144	−0.2477
C	0.350	0.276144	−0.0357
C	0.350	0.276144	−0.2471
C	0.350	0.276144	−0.0016
C	0.350	0.276144	−0.3275
H	0.250	0.12552	0.1151
H	0.250	0.12552	0.1151
H	0.250	0.12552	0.1046
H	0.250	0.12552	0.1046
H	0.250	0.12552	0.1046
H	0.250	0.12552	0.1043
H	0.250	0.12552	0.1043
H	0.250	0.12552	0.1069
H	0.250	0.12552	0.1069
H	0.250	0.12552	0.1069
H	0.250	0.12552	0.1349
H	0.250	0.12552	0.1349
H	0.250	0.12552	0.1147
H	0.250	0.12552	0.1147

H	0.250	0.12552	0.1147
Li_subs			
Li	0.280	9.00	0

366

367

References

[S1] Wang, Z. *et al.* Non-flammable ester electrolyte with boosted stability against Li for high-performance Li metal batteries. *Angew. Chem. Int. Ed.* **134**, e202206682 (2022).

[S2] Zeng, Z. *et al.* Non-flammable electrolytes with high salt-to-solvent ratios for Li-ion and Li-metal batteries. *Nature Energy* **3**, 674-681 (2018).

[S3] Zhang, X. *et al.* A dicarbonate solvent electrolyte for high performance 5 V-Class Lithium-based batteries. *Nat. Commun.* **15**, 536 (2024).

[S4] Chen, J. *et al.* Highly Reversible Lithium-Metal Anode and Lithium–Sulfur Batteries Enabled by an Intrinsic Safe Electrolyte. *ACS Applied Materials & Interfaces* **11**, 33419-33427 (2019).

[S5] Yang, C. *et al.* Engineering A Boron-Rich Interphase with Nonflammable Electrolyte toward Stable Li||NCM811 Cells Under Elevated Temperature. *Adv. Mater.* **36**, 2307220 (2024).

[S6] Holoubek, J. *et al.* An All-Fluorinated Ester Electrolyte for Stable High-Voltage Li Metal Batteries Capable of Ultra-Low-Temperature Operation. *ACS Energy Letters* **5**, 1438-1447 (2020).

[S7] Xu, J. *et al.* Electrolyte design for Li-ion batteries under extreme operating conditions. *Nature* **614**, 694-700 (2023).

[S8] Cho, S.-J. *et al.* Nonflammable lithium metal full cells with ultra-high energy density based on coordinated carbonate electrolytes. *Iscience* **23** (2020).

[S9] Chen, S. *et al.* High-efficiency lithium metal batteries with fire-retardant electrolytes. *Joule* **2**, 1548-1558 (2018).

[S10] Zheng, Q. *et al.* A cyclic phosphate-based battery electrolyte for high voltage and safe operation. *Nature Energy* **5**, 291-298 (2020).

[S11] Xiao, L. *et al.* Stable Li metal anode with “ion–solvent-coordinated” nonflammable electrolyte for safe Li metal batteries. *ACS Energy Letters* **4**, 483-488 (2019).

[S12] Sun, H. *et al.* High-safety and high-energy-density lithium metal batteries in a novel ionic-liquid electrolyte. *Adv. Mater.* **32**, 2001741 (2020).

[S13] Wu, F. *et al.* Dual-anion ionic liquid electrolyte enables stable Ni-rich cathodes in lithium-metal batteries. *Joule* **5**, 2177-2194 (2021).

[S14] Fan, X. *et al.* All-temperature batteries enabled by fluorinated electrolytes with non-polar solvents. *Nature Energy* **4**, 882-890 (2019).

[S15] Yuan, S. et al. Advanced Electrolyte Design for High-Energy-Density Li-Metal Batteries under Practical Conditions. *Angew. Chem. Int. Ed.* **60**, 25624-25638 (2021).

[S16] Lee, S. *et al.* Safe, stable cycling of lithium metal batteries with low-viscosity, fire-retardant locally concentrated ionic liquid electrolytes. *Adv. Funct. Mater.* **30**, 2003132 (2020).

[S17] Fan, X. *et al.* Non-flammable electrolyte enables Li-metal batteries with aggressive cathode chemistries. *Nature nano.* **13**, 715-722 (2018).

[S18] Sambasivarao, S. V. & Acevedo, O. Development of OPLS-AA Force Field Parameters for 68 Unique Ionic Liquids. *Journal of Chemical Theory and Computation* **5**, 1038-1050 (2009).

[S19] Doherty, B., Zhong, X., Gathiaka, S., Li, B. & Acevedo, O. Revisiting OPLS Force Field Parameters for Ionic Liquid Simulations. *Journal of Chemical Theory and Computation* **13**, 6131-6145 (2017).

[S20] Luo, P. et al. Ternary-salt localized high-concentration electrolyte: An ideal companion facilitating stable high-voltage cycling of lithium metal batteries. *J Energy Storage* **102**, 114197 (2024).

[S21] Zhang, G. et al. A nonflammable electrolyte for high-voltage lithium metal batteries. *ACS Energy Lett*. **8**, 2868-2877 (2023).

[S22] Liu, Q. et al. An Inorganic-Dominate Molecular Diluent Enables Safe Localized High

Concentration Electrolyte for High-Voltage Lithium-Metal Batteries. *Adv. Funct. Mater.* **33**, 2209725 (2023).

[S23] Zhu, J. et al. Practical High-Voltage Lithium Metal Batteries Enabled by the In-Situ Fabrication of Main-Chain Fluorinated Polymer Electrolytes. *Angew. Chem. Int. Ed.* **2025**, e202424685 (2025).

[S24] Peng, X., Lin, Y., Wang, Y., Li, Y. & Zhao, T. A lightweight localized high-concentration ether electrolyte for high-voltage Li-Ion and Li-metal batteries. *Nano Energy.* **96**, 107102 (2022).

[S25] Yang, Y.-P. et al. Thermal stability analysis of lithium-ion battery electrolytes based on lithium bis (trifluoromethanesulfonyl) imide-lithium difluoro (oxalato) borate dual-salt. *Polymers* 13, 707 (2021).

[S26] Jamil, S. et al. Ni/Li antisite induced disordered passivation layer for high-Ni layered oxide cathode material. *Energy Storage Mater.* **45**, 720-729 (2022).

[S27] Lin, T. et al. Faster activation and slower capacity/voltage fading: a bifunctional urea treatment on lithium‐rich cathode materials. *Adv. Funct. Mater.* **30**, 1909192 (2020).